Deformation mechanics in inclined, brittle-ductile transpression zones: insights from 3D finite element modelling

Seyed Tohid Nabavi

Faculty of Earth Sciences, Department of Geology, Shahid Beheshti University, Tehran, Iran, Tel.: +989112914581, E-mail: tohidnabavi@gmail.com; T_nabavi@sbu.ac.ir

Seyed Ahmad Alavi

Faculty of Earth Sciences, Department of Geology, Shahid Beheshti University, Tehran, Iran

Manuel Díaz-Azpiroz

Departamento Sistemas Físicos, Químicos y Naturales, Universidad Pablo de Olavide, Crtra, Utrera, km 1, 41013, Seville, Spain

Soheil Mohammadi

High Performance Computing Laboratory, School of Civil Engineering, University of Tehran, Tehran, Iran

Mohammad Reza Ghassemi

Research Institute for Earth Sciences, Geological Survey of Iran, Tehran, Iran

Carlos Fernández

Departamento de Ciencias de la Tierra, Universidad de Huelva, Campus de El Carmen, 21071, Huelva, Spain

Leticia Barcos

Departamento Sistemas Físicos, Químicos y Naturales, Universidad Pablo de Olavide, Crtra, Utrera, km 1, 41013, Seville, Spain

Marcel Frehner

Zurich University of Teacher Education (PHZH), Zurich, Switzerland

Abstract

Most natural examples of transpression zones developed at oblique convergence regime are inherently 3D and have inclined boundaries. A 3D finite element model with an elasto-plastic rheology is used to investigate the structural and mechanical evolution of inclined transpression zones in a rock sequence above a frictional basal detachment. Inelastic constitutive relationships allows permanent strains to develop in response to the applied loads. FE-modelling results show that oblique convergence is accommodated by discrete deformation at the main pre-existing inclined faults (=70°) and by distributed brittle and ductile deformation at active blocks. Oblique contraction at the active blocks resulted mainly in layer-parallel shortening, orthogonal to the model outer boundaries, whereas thickening in the horizontal and vertical directions was accommodated via layer-parallel, fault strike-parallel extension and up-dip extrusion (i.e., inclined extrusion). Lateral extrusion should have compensated the rest and/or volume loss took place. Folding and thickening of the mobile backstop produced a non-cylindrical, asymmetric, bi-vergent anticline where permanent strains developed principally in the steep forelimb. Secondary, conjugate fault zones also accommodate oblique slip and contribute to uplift. Displacement vectors within the transpression zone are rotated counter-clockwise (ca. 20°-30°) with respect to vectors in the fixed backstop. Areas with higher rotation values seem to correlate with those showing higher ellipticity values. The presence of pre-existing faults favored strain partitioning from the onset of deformation. FE-modelling results compared with analytical, natural example, and analogue modelling results show that our mechanical modelling can overall match inclined transpression zones geometry that present different modes of strain partitioning and localisation.

Keywords: Oblique convergence, Inclined transpression, Inclined extrusion, Strain partitioning, 3D Finite-element modelling

1. Introduction

Transpression (and transtension) kinematics derives from obliquity between velocity vectors and boundaries between deforming crustal blocks, an inevitable consequence of the rotational character of plate tectonics (Harland, 1971; Dewey et al., 1998; Díaz-Azpiroz et al., 2016; Philippon and Corti, 2016). Oblique convergence produces transpressional deformation in many different tectonic settings, including fold-and-thrust belts (e.g., Sarkarinejad et al., 2013; Barcos et al., 2015; Li et al., 2018), mountain ranges (e.g., Nabavi et al., 2017b; Malavielle et al., 2019), accretionary wedges (e.g., Schulmann and Gayer, 2000) or intraplate deformation zones (e.g., Bradley et al., 2017; van Gelder et al, 2017). Kinematically, transpression zones form from the simultaneous operation of two components, simple shearing and coaxial flow (Fossen and Tikoff, 1993; Fernández and Díaz-Azpiroz; 2009; Frehner, 2016; Fossen and Cavalcante, 2017) resulting in non-plane strain. In this regard, the study of transpression (and transtension) zones helps us to better understand crustal 3D kinematics, as deduced from many field-based studies (e.g., Díaz-Azpiroz and Fernández; 2005; Zanchi et al., 2016; Nabavi et al., 2017b, 2017c; Simonetti et al., 2018; Bergh et al., 2019; Alonso-Henar et al., 2020), as well as analytical (e.g., Fossen et al., 1994; Fossen and Tikoff, 1998; Jones et al., 2004; Jiang, 2007; Fernández and Díaz-Azpiroz; 2009), analogue (e.g., Tikoff and Peterson, 1998; Casas et al., 2001; Leever et al., 2011; Ghosh et al., 2014; Barcos et al., 2016; Sadeghi et al., 2016), and numerical (e.g., Davis et al., 2013; Nevitt et al., 2014, 2017; Dasgupta et al., 2015; Frehner, 2016; Nabavi et al., 2017a, 2018a, 2018b, 2019) models. In essentially ductile transpressional zones both simple shearing and coaxial flow are commonly present within the entire shear zone producing complex finite deformation geometries (e.g., Alsop et al., 1998; Vitale and Mazzoli, 2008, 2015; Davis and Titus, 2011; Fernández et al., 2013; Fossen and Cavalcante, 2017; Carreras and Druguet, 2019). In contrast, brittle-ductile shear zones usually show significant strain partitioning producing separate, large-scale deformational domains

characterized by different kinematics (Tikoff and Teyssier, 1994; Curtis, 1998; Schulmann et al., 2003; Jones et al., 2005).

Some natural shear zones have monoclinic symmetries, with strike- and/or dip-parallel lineations. However, many other cases have variably oriented oblique lineations (e.g., Hudleston et al., 1988; Sullivan and Law, 2007), which cannot be explained by monoclinic models. Such shear zones are more realistically modelled by transpression with triclinic symmetry (e.g., Robin and Cruden, 1994; Lin et al., 1998; Czeck and Hudleston, 2003, 2004; Iacopini et al., 2007; Horsman et al., 2008; Fernández and Díaz-Azpiroz, 2009; Viola and Henderson, 2010; Toy et al., 2013; Xypolias et al., 2018). Triclinic transpression can be reproduced by horizontal velocity vectors acting on inclined shear zone boundaries, which was termed 'inclined transpression' (Dutton, 1997), and can be depicted in a 'strain triangle' (Jones et al., 2004; Díaz-Azpiroz et al., 2014).

Moreover, most oblique convergence settings are horizontally and vertically heterogeneous in their constitutive properties, which affect the structural style and deformation mechanics. Therefore, the structural style and fault systems patterns in natural transpressive (or transtensional) zones are controlled, in addition to the convergence angle, by the orientation of the mechanical layering with respect to the strain field, the relative orientation of pre-existing faults, and the coefficient of sliding friction on the fault plane (Bott, 1959; Hughes et al., 2014; Hughes and Shaw, 2015; Ferrill et al., 2017; Nabavi et al., 2017a, 2018a). Mechanical stratigraphy causes non-uniform deformation of multilayer systems when subjected to tectonic stress (e.g., Treagus, 1993; Gómez-Rivas and Griera, 2012). Mechanical stratigraphy contains different ranges of material heterogeneity and anisotropy such as layered units (competent and incompetent layers), the presence of bedding-plane discontinuities (Cooke and Underwood, 2001; Bourne, 2003; Bose et al., 2018), the thicknesses of the mechanical layers, tensile strengths (range from 2 to 40 MPa, Bieniawski, 1984), the compressive strengths (from 30 to

350 MPa, Bieniawski, 1984), the Young's modulus (from about 1 to 100 GPa, Eschbac, 1961; Bayerlee, 1970), the character and frictional properties of the transitions or, the confining stress at the brittle and ductile deformation (range between 30 and 300 MPa, Jaeger et al., 2007). These factors cause the wide range of geological structures and influence on their evolution (e.g., fold formation, failure mode, fault geometry and growth, spacing of fractures/faults, displacement distribution and gradient, dip of slip surfaces, fault zones width, etc.; see McClay et al., 2004; Ferrill and Morris, 2008; Ferrill et al., 2017; Michie et al., 2014; McGinnis et al., 2016; Boersma et al., 2020).

In this study, we present, for the first time, a non-linear 3D FE-model that simulates the deformation mechanics in an inclined (thus triclinic) transpression zone affecting an alternating brittle-ductile-brittle sedimentary cover frictionally detached from a competent rock basement. In addition, it is important to note that we use non-rigid deformation zone boundaries and backstops. The terminology used to convey the lithostratigraphic influence on structural style includes lithotectonic units (Jacobeen and Kanes, 1975) and structural-lithic units (Woodward and Rutherford, 1989). The presented model is purposely simplistic. Geological processes, such as diagenesis, erosion, fluid flow, temperature, etc. are not considered. The primary reason for this approach is that we seek to isolate the effects of a few selected parameters, such as material properties, oblique convergence and fault geometry in order to keep the analysis tractable. While the effect of additional processes could be investigated, they would produce a wide range of even more complex structural geometries, and thus would increase the difficulties in providing unambiguous interpretations of the results.

Our results are focused on (1) geometry, kinematics, and mechanics of structural deformation, (2) variation of slip along fault segments, and (3) spatial variation of the displacement vectors, so that we attempt to address: (i) the importance of oblique convergence in the deformation patterns of inclined transpression developed in upper crustal conditions

(with frictional detachment and plastic interlayers), (ii) the influence of mechanical stratigraphy in the construction of the transpression zone, (iii) the possible trends for strain refraction across different layers in the transpression zone, (iv) the implications of strain results in the prediction and development of probable brittle and ductile structures within the transpression zone, and (v) the effects of inherited structures in the strain partitioning and the geometry of the resulting wedge. In the discussion section, insights from FE-model results in strain partitioning are investigated and linked to the analytical, kinematic, analogue, and numerical models established before. Our approach is general; hence, its conclusions are independent from the specific structural geometry and can be then applied to other examples and tectonic settings.

2. Model setup

The numerical model is based on the concept of continuum mechanics and the governing system of partial differential equations is solved numerically with the finite element method. The general purpose FE-ABAQUS™ commercial code (ABAQUS/CAE; FE-commercial program ABAQUS™ tutorial version 6.14-2, 2014; www.simulia.com/) was selected for this study because it is well suited to analyse geomechanical problems over a wide range of scales in 1, 2, and 3D. ABAQUS™ employs a Lagrangian formulation that accurately handles large strains and rotations as well as complex contact interfaces with frictional behaviour where significant sliding can occur. It also has efficient algorithms for solving highly non-linear problems that result from both geometric complexity and material behaviour. In addition, ABAQUS™ has a large flexibility of model constitutive relationships that are appropriate for simulating the behaviour of rocks, ranging from simple elastic material models to advanced elastic-plastic (e.g., Mohr-Coulomb, Drucker-Prager, Damage mechanics) and visco-elastic material models.

The proposed model (Fig. 2) comprises an upper, three-layered block that slides frictionally on top of a rigid basement. The upper block is segmented by two dipping, parallel fault planes into three blocks, which are called here 'active' blocks. The coordinate system is defined by a horizontal XY plane, with the X-axis parallel to the strike of the fault planes, and a vertical Z-axis (Fig. 2a). The rigid block is 5.5 km thick whereas the upper, middle, and lower layers of the 'active' blocks are 3, 1.5 and 5 km thick, respectively (Fig. 2a, b). The lateral dimensions of the 'active' block are 75.5×50×9.5 km and the two faults, planar and mutually parallel, are 50 km long, dip 70° and end at tip lines (Fig. 2a, b). Additionally, the sidewalls and the upper surface were unhindered, so that displacement along the fault planes is allowed both horizontally (along the X-axis) and up-dip (Y- and Z-axis), thus resulting in oblique-slip faults in the analysis. These faults were simulated with frictional sliding interfaces that employ a classic Mohr-Coulomb friction model, with a 0.6 friction coefficient assigned to the fault interfaces. The deforming material between faults is allowed to shorten (or lengthen), and shear vertically and horizontally.

The rheology of the upper crust is elasto-plastic, which means that stresses increase with strain up to a certain limit, where failure occurs and plastic deformation starts. Furthermore, elasto-plastic models usually provide the most reliable representations of shallow faulting behaviour. In this regard, an elasto-plastic constitutive law was implemented with the elastic component assumed to be linear isotropic by assigning Mohr-Coulomb plasticity. This constitutive definition introduced six model parameters into the analysis: Young's modulus (E), Poisson's ratio (υ), gravitational acceleration (g), rock cohesion (C), rock internal friction (ϕ), and basal friction (μ). The material properties of the three active block layers are, from up to bottom, elasto-plastic limestones with an elastic modulus of 48 GPa, a Poisson ratio of 0.25, and a density of 2700 kg/m^3, plastic marls with an elastic modulus of 0.2 GPa, a Poisson ratio of 0.2, and a density of 2100 kg/m^3, and another elasto-plastic limestone layer (based on Carmichael,

1982; Pollard and Fletcher, 2005; Jaeger et al., 2007). The contacts between layers in the deforming block have been modelled as glued contacts. Other material properties used in this study are shown in Table 1. These inelastic material model permits permanent strains to develop in response to the applied oblique load. This model setup, with a frictional detachment and weak layers interbedded within the sequence, would resemble a common stratigraphic configuration found in various fold-and-thrust belts, such as the Dezful Embayment in the Zagros belt (e.g., Ruh et al., 2017; Derikvand et al., 2018; Sarkarinejad et al., 2018) or the eastern Jura belt (e.g., Malz et al., 2016; Nussbaum et al., 2017), as well as in some orogenic basins, such as the Malargüe group in the Neuquén basin, Argentina (Balgord and Carrapa, 2016).

Oblique convergence is modelled by imposing a given displacement (Fig. 2) to the active upper block. Block 1 is fixed in all directions (i.e., an encastre boundary condition), block 3 is the mobile backstop and block 2, bounded by the two dipping faults, represents an inclined transpressional zone (Fig. 2). A regional oblique shortening of 16% (3 km shortening) is imposed along the outer boundary of the mobile backstop under a convergence angle (angle α between the imposed convergence vector and the line perpendicular to the transpression zone boundary) of 25° (Fig. 2a, c), resulting in a pure shear-dominated transpression. Imposing displacements, instead of traction, allows formulating a model that is consistent with field observations and obviates the need to infer stresses (Fig. 2). The model width (along the X-axis) is constant during oblique convergence. Numerically, free surface boundary conditions are applied on the top model face, thus permitting self-consistent evolution of topography. In addition, both lateral boundary conditions are defined as free-slip along the boundary planes (Fig. 2c). Acceleration due to gravity (9.81 m/s^2) is imposed throughout the deformation as a body force. Due to the presence of the mechanical layering and inclined boundaries within the model blocks, we chose the recommended automatic time increment option in ABAQUS™. A

choice of maximum and minimum allowable time increments of 0.01 for a total model time of 1.00 unit ensures that ABAQUS^{TM} will choose a computationally efficient step size. This also ensures that the model output is written close to selected increments of interest (for example, every 0.1 units of time). The finite element mesh for the entire upper deforming block comprises 15,032 modified hexahedron elements having eight corner nodes. These elements are recommended for complex three-dimensional contact analysis in ABAQUS^{TM}. Mesh resolution was 1 km, which was determined by comparing results among multiple meshes created with different element size ranging from 600 m to 1.5 km and model geometries. The choice of element size was a compromise between output resolution and computational efficiency. According to the 3D nature of the study model, each interior node has three degrees of freedom. We utilized reduced-integration hexahedral plane strain elements that conform to the predefined surface-to-surface contacts and reduced stress artefacts arise from frictional slip.

We use the 3D FE-modelling to simulate stress and strain features recorded in the transpression zone. Due to the continuum nature of the FE-analysis, the model presented here cannot simulate the brittle failure of rocks, characteristic of shallow crustal levels. However, by using the orientation of the principal stresses and strains that develop in the modelled transpression zone, it is possible to show and predict the most probable orientation of brittle structures that could develop during deformation.

3. Results

In this Lagrangian model, the meshes are deformed reproducing crustal blocks and material deformation.Oblique convergence, pre-existing inclined faults, mechanical stratigraphy and the nature of the frictional detachment horizons (lower frictional detachment at the base and intermediate viscous detachment at the marl layer) play significant roles in the structural evolution, strain localisation, importance of brittle and ductile structures, and spatial

distribution of deformation along and across the inclined transpression zone. Under oblique convergence, ductile deformation localises preferentially within the transpression zone bounded by the two dipping faults and in block 3. Upon imposing the total oblique convergence in an incremental manner, the model block evolves under a combination of slip (discrete deformation) on the faults and distributed deformation within the 'active' blocks. The 'active' blocks overall undergo oblique contraction, which results in shortening, and thickening in the horizontal and vertical directions, respectively. It is important to note that uplift and subsidence develop in our models only as a result of the amount of oblique convergence, and other processes such as sedimentation, and isostatic response have not been considered. This is a simplification, as these processes are known to affect uplift and subsidence. We expect, however, that the general pattern of surface deformation is accurate.

3.1. Geometry, kinematics and mechanics of the modelled inclined transpression zone

The FE-model results presented in this study are orientation and magnitude of plastic strain, shear strain, displacement, and stress (Figs. 3 to 8). We use this information to predict the most probable location, orientation and behavior of real structures (folds and faults) that would develop during deformation.

Deformation throughout the experiment affects the three active blocks albeit differently (Fig. 3). A wedge-shaped deformed volume (positive flower-shaped structure) formed at the central part of the model, completely affecting block 2, and whose limits are located at blocks 1 and 3. The mobile backstop (block 3) was deformed more intensively than the fixed one (block 1), and plasticity developed over a total distance of about 12 km within active blocks (Fig. 6). This wedge-shaped zone entirely accommodated the transpressional deformation imposed by the oblique convergence boundary conditions, via slip on arrays of faults and the development of systematic minor fold sets as penetrative strain (cf., Burberry, 2015). Layers

248 in the mobile backstop were tilted and flexed upward above fault 2. An inclined, tabular-shaped
249 transpressional zone formed in block 2 bounded by the two parallel pre-existing faults (faults
250 1 and 2) (Figs. 3 and 6d).

251 Oblique convergence at the model was accommodated by discrete deformation (simple
252 shearing/slip) at the two main pre-existing faults and by distributed brittle and ductile
253 deformation at active blocks, localised preferentially at the tabular-shaped transpression zone.
254 Maximum incremental strains were concentrated at this transpressional zone and particularly
255 at its boundaries, although fault 2 presents higher strain values (=1.3-2.6) than fault 1 (=0.8-
256 1.3).

257 Stress and strain orientations and magnitudes during the experiment suggest that oblique
258 contraction at the active blocks resulted mainly in layer-parallel shortening (parallel to the Y-
259 axis), compensated by lengthening in the horizontal (X-axis parallel) and vertical directions,
260 respectively accommodated via layer-parallel extension and up-dip extrusion mainly produced
261 at the frontal part of the two main oblique faults (Figs. 3 and 6). This heterogeneous thickening
262 results from increased normal stress across the inclined fault boundaries at depth (Fig. 4), which
263 causes distributed deformation. At the end of the experiment, after 3 km of backstop oblique
264 convergence, 16% of orthogonal shortening was compensated by 40% of vertical extrusion (the
265 total thickness increased from 9.5 to 13.2 km). Shortening at the tabular transpression zone and
266 lateral extrusion (~28%) should have compensated the rest of oblique convergence, and/or
267 volume loss with penetrative strain took place. Overall, the wedge-shaped zone was deformed
268 by plunging oblique folds, oblique-slip faults, thrust stacks and distributed distortion within the
269 inclined transpression zone (Figs. 3 to 6). The main structures are described in detail in the
270 following paragraphs.

271 According to the strain distribution, we can identify three fault types in the wedge-shaped
272 zone (Figs. 3 and 6d): (i) the main dipping thrusts (i.e., forethrusts or pro-shears in Leever et
273 al., 2011), localised here at the pre-existing inclined faults and also at the fixed block; (ii)
274 oblique shear bands at the tabular zone that cross-cut bedding planes; and (iii) backthrust planes
275 (pro-wedge thrust faults or retro-shears in Leever et al., 2011) that develop within the mobile
276 backstop due to a local contractional bend (the type-I backthrust model in Xu et al., 2015), and
277 also the transpression zone. Pro-shears in the fixed block have smaller dip angles (~20-35°)
278 than backthrusts (~40-50°) and the main oblique shears (~65°) (Fig. 3). In general, fore- and
279 backthrusts were more penetrative in competent layers (limestone layers) than in the
280 incompetent layer (marl). Slip on the fault planes is oblique and faults exhibit dip refraction as
281 a function of the lithology. In the limestone (more brittle) and marl (less brittle) layers, faults
282 dip 65-80° and 40-55°, respectively (Fig. 4). A forethrust or footwall shortcut thrust (Fig. 3) is
283 a characteristic feature of basins under tectonic shortening. This leads to the footwall shortcut
284 thrust faults to break off from the original high angle to a lower angle towards the surface
285 (Powell, 1987; McClay and Buchanan, 1992).

286 Regarding the tabular, inclined transpressional zone of block 2, horizontal and vertical
287 displacement of material caused the oblique (dextral-reverse) simple shearing along the
288 bounding faults (faults 1 and 2), as seen by the asymmetric distribution of shear stress/strain
289 (Fig. 7a). These two faults accumulate large amounts of strain (higher value of incremental
290 shear strain), although fault 2 accommodates higher shear strain values, and it is considered
291 more active, than fault 1. Secondary, conjugate fault zones also accommodate oblique slip and
292 contribute to uplift. Much smaller strains are accumulated at the backthrust, which propagates
293 upwards from the basal detachment, and the shear bands (cross-cutting bedding planes) of the
294 wedge.

295 Dextral-reverse slip on faults 1 and 2 creates offset between the model blocks. It also causes
296 the displacement vectors (or particle paths in the XY horizontal plane) within this
297 transpressional zone to rotate counter-clockwise with respect to vectors in the undeformed
298 sector, forming a ca. 20-30° angle with the backstops (Fig. 8b). The final top view architecture
299 of the model reveals that this oblique fault system deviates from the linear trend reproduced in
300 orthogonal experiments (e.g., Marques and Nogueira, 2008; Graveleau et al., 2012 and
301 references therein) and attains a somewhat curved trend. Overall, a variety of damage zones,
302 particularly interaction, wall, and distributed damage zones (see Peacock et al., 2017 for details
303 of damage zones) are developed as a result of oblique convergence throughout the transpression
304 zone.

305 Fold hinges plunge and are not straight, so that folding and thickening of the mobile
306 backstop (block 3) produced a non-cylindrical, asymmetric, bi-vergent anticline (hangingwall
307 anticline or pop-up structure), which is flanked by oblique thrusts with permanent strains
308 developed principally in the steep forelimb (or retro-wedge) (Figs. 3 and 4). This pop-up
309 structure was bounded by an oblique backthrust at block 3 and one of the pre-existing oblique
310 faults (fault 2) (Fig. 6). The shear strain is high in the front of this asymmetric anticline (close
311 to fault 2) and progressively decreases toward the trailing parts of the mobile backstop. This
312 strain asymmetry is the result of the basal boundary condition and the tip line of the pre-existing
313 inclined fault, and likely produced an 850 m-high scarp at the front of this anticline.

314 Deformation also causes tilting at the inclined fault 2 edge and steepening of the anticline
315 backlimb due to limb rotation with hinge migration, a common feature in transpressional
316 folding (Tikoff and Peterson, 1998; Titus et al., 2007). Frehner (2016) showed that the fold
317 hinges are not passive material lines, but active markers that migrate during transpression. This
318 anticline would have been favored by the frictional surface between the active blocks and the
319 basic rigid block, and the presence of an inclined fault plane (fault 2). The fold would contribute

to the tectonic thickening of the hangingwall (cf. Koyi and Maillot, 2007). The anticline is linked with a syncline towards the rear of the displacement block 3, and the whole structure could be considered as a 'concave fault bend fold' (Brandes and Tanner, 2014; Ziesch et al., 2014). However, unlike the fault-parallel flow model due to pure contraction (Ziesch et al., 2014), here, the flow path is oblique to the inclined fault. In this regard, different structural styles occur at the active blocks, such as pressure solution cleavages, backthrusts and extensional fractures depending on stress boundary conditions and mechanical stratigraphy. Moreover, cross-sections across the study model (Fig. 4) show that the mechanical stratigraphy influences folding geometries, so that more brittle layers (limestone layers) lead to more rounded fold geometry whereas less brittle layer (marl layer) lead to sharp-hinged and flat-topped fold geometry. Also, the lower limestone layer shows wider hinge zones than the upper limestone layer due to increases in thickness and depth (Fig. 4).

As oblique convergence increases, inclined transpression is accommodated by progressively greater slip at the pre-existing faults while the anticline in the mobile backstop grows by increasing its amplitude rather than its width. Furthermore, the tabular-shaped transpression zone progressively rotates cause the anticline to rotate progressively from upright to overturned. This rotation is accompanied by stretching and thinning of the forelimb, which can causing local strain partitioning (e.g., Carreras and Druguet, 2019). Therefore, this deformation generates local asymmetric synclines verging toward the fixed backstop (Figs. 3 and 4).

Compressive stress developed in the tabular-shaped transpressional zone and the non-cylindrical, asymmetric anticline, where the three principal stress axes are oblique with respect to the pre-existing faults (transpression zone boundaries) (Fig. 5). The principal axes of the stress tensor rotate in these zones (Fig. 5), such that the value of the horizontal stress decreases enough for tension to occur close to the outer arc of the uplifted areas.

3.2. Variation of slip along inclined fault segments

According to high maximum values of shear (=5.57e^7 Pa) and normal (=4.39e^8 Pa) stresses on sliding surfaces (Fig. 7a, b), slip can occur along fault 2, although relatively low friction coefficient (< 0.2) is required. Moreover, the slip tendency (i.e., the ratio of resolved shear and normal stresses acting on the fault surface, Morris et al., 1996) is relatively low (=0.13). This low value is due to the existence of the high angle ramp and the stress localisation at the fault interface, such that the fault acts as a mechanical heterogeneity. Moreover, the upper limestone layer shows a higher value of the intermediate normal stress than the lower limestone layer (Fig. 4), which may be related to the incompetent marl layer between them and the thickness of the lower limestone layer. In general, steep fault segments (dip angle > 60°) through competent units such as limestone, have lower slip tendency than gentler fault segments (dip angle < 60°) because of the lower resolved shear stress acting on those steep surface segments (see Ferrill et al., 2017; Rosas et al., 2017 for details). Introducing elasto-plastic rheology results in markedly different and asymmetric slip distribution along the inclined fault surfaces, with more slip reaching the sub-surface and greater localisation (Fig. 7c, d). On the other hand, model results indicate shallow faulting is also associated with mechanical layering and plastic yielding. Given that new faults form during progressive oblique convergence, the main oblique-reverse faults (i.e., transpression zone boundaries) with higher slip tendencies are represented by multiple and asymmetric displacement values from high to low. Morris et al. (2016), in line with this subject, proposed a conceptual form of the nonlinear relationship between slip tendency and the observed fault displacement (fig. 7 in Morris et al., 2016). It should be noted that the regions for higher slip tendency overlap with areas of volume loss or dilation tendency, suggesting that faults/fractures could be developed as a mixed-mode failure type (e.g., Stephens et al., 2017).

3.3. Spatial variation of the displacement vectors across the model

Model results show that the resultant displacement leads to the final surface topography after shortening by 16%. As the model block (crust) is converged above the inclined boundary, it bulges and forms the inclined transpression (or orogenic belt in crustal-scale) of elevated topography. Indeed, we present here a displacement map for the study model. During model oblique convergence, displacement vectors (Fig. 8b, c) show: *(i)* The X component gradually vanishes away from the applied far-field stress, with a clear step at the oblique-reverse fault 1; *(ii)* The Z component increases from the bottom to the top, and gradually vanishes away from hagingwall-anticline; *(iii)* In the hangingwall blocks, displacement vectors rotated from horizontal near applied stress's boundary toward higher dip angles till they become slightly oblique to sub-parallel to the transpression zone boundaries (Fig. 8b). In the footwall block, the X component decreases and displacement vectors show an almost pure Y component; *(iv)* Shortening was accommodated by layer thickening and displacement along both oblique-reverse faults; *(v)* The map integrating displacement show the curvilinear (non-linear) pattern in the hangingwall block and transpression zone (Fig. 8b), with trajectories dipping around 20-30° in hangingwall block, and 35-50° in the transpression zone, thus oblique to the transpression zone boundaries (Fig. 8c). Furthermore, displacement vectors at the base of the hangingwall block and the transpression zone dips < 5°, and are thus sub-horizontal (Fig. 8c) (e.g., analogue model with the 70° dipping indenter in Cruz et al., 2008); *(vi)* Displacement in the footwall blocks immediately below the transpression zone boundary was parallel to the Y axis and sub-horizontal (Fig. 8b, c); *(vii)* On the left side of the inclined transpression zone (map view) (Fig. 8b), the displacement vectors have an increasing component of lateral displacement in the direction of the weak lateral component, i.e., vectors deviate from the convergence direction and rotate towards the weak lateral component as lateral extrusion; *(viii)*

393 The displacement partitions into various amounts of up-dip extrusion (as non-cylindrical fold)
394 and heterogeneous strain throughout the transpressional system.

395 ## 4. Discussion

396 ### 4.1. Deformation of the model

397 The purpose of the mechanical models in this study is not to simulate the exact geometry of
398 the deformation structures documented in specific natural examples but to contribute to a
399 general understanding of the basic mechanical processes and the kinematic regime that might
400 have influenced their development. The numerical results present a strain partitioning pattern
401 characterised by two main domains, each of which accommodated different components of
402 transpressive deformation. Narrow domains at the two pre-existing faults accommodated
403 simple shear-dominated dextral transpression whereas a wide domain deformed by pure shear-
404 dominated triclinic transpression.

405 In the wide, pure shear-dominated domain, the displacement was partitioned between
406 mainly dextral and dextral-reverse faults sub-parallel with the main boundaries, and reverse
407 faults and associated folds obliquely oriented (0-30°) to them (i.e., axial length of fold is
408 oblique to the boundaries and the fixed backstop). This agrees with results from other kinematic
409 and analogue models (e.g., Casas et al., 2001; Leever et al., 2011; Díaz-Azpiroz et al., 2014;
410 Barcos et al., 2015; Calignano et al., 2017). The trend of the transpression zone is parallel with
411 the backstops and shortening and related oblique lateral extrusion (25-40° with respect to the
412 main inclined transpression zone boundaries) is produced by oblique-reverse faults and folds.
413 Folds show no evidence of rotation in either model. This seems to differ from other cases of
414 folding in monoclinic transpression zones simulated by analytical (e.g., Tikoff and Teyssier,
415 1994; Titus et al., 2007), analogue (Tikoff and Peterson, 1998; Ghosh et al., 2014), and
416 numerical modelling (Frehner, 2016; Nabavi et al., 2018a) in which folds rotate or

417 accommodate to finite strain axes re-orientation during progressive deformation. Fold axes in
418 the FE-model follow a curved path and takes place mainly by hinge-parallel extension and
419 elongated markers. Stretching parallel with the X-axis is accommodated by the principal strike-
420 slip faults. Transpression zone-parallel stretch and oblique shortening, both resulting from the
421 coaxial flow component, would lead to space problem and strain incompatibility (e.g., Vitale
422 and Mazzoli, 2008), unless they are accommodated by lateral and/or up-dip extrusion (e.g.,
423 Fernández and Díaz-Azpiroz, 2009; Sarkarinejad et al., 2009; Mukherjee and Koyi, 2010;
424 Viola and Henderson, 2010; Mukherjee et al., 2012), which is the case of the study model.

425 Lateral extrusion entails the combined effects of material (or tectonic) escape and
426 gravitational collapse of a weak wedge in response to oblique convergence under conditions of
427 inclined and lateral boundaries so that extrusion is oriented at a high angle to the convergence
428 direction (Fig. 8b) (e.g., Ratschbacher et al., 1991; van Gelder et al., 2017). The highest degree
429 of lateral extrusion occurs near the fixed backstop boundary (fault 2, Fig. 8b). Following such
430 lateral extrusion, some local oblique-reverse faults and shear zones develop in that area,
431 spatially related to vertical to overturned fold limbs, so that their orientation and vergence are
432 similar (Fig. 8b, d). In this regard, important parameters influencing the extrusion (amount and
433 orientation) and the resulting deformation patterns are the dip of boundaries, the angle of
434 oblique convergence, the mechanical stratigraphy, the amount of convergence and the width of
435 the contracted zones.

436 Additionally, deformation in the brittle layers is mainly accommodated by thrust faults,
437 which are spatially related to thickening in the underlying ductile layer, suggesting high
438 mechanical coupling. Furthermore, the results show that low shear strain and shear stress are
439 necessary for backthrusts and shear bands to form (e.g., Ruh et al., 2012, 2014). Using critical
440 taper theory it has been shown that backthrusts preferentially form at low taper angles. For
441 medium obliquities ($\alpha \leq 45\text{-}55°$), thrust faults dips are steeper and their number is lower in

oblique convergence than in purely frontal convergence deformation styles (e.g., Richard and Cobbold, 1990; McClay et al., 2004; Graveleau et al., 2012; Xu et al., 2015; Bose and Mukherjee, 2019).

4.2. Strain partitioning in transpression

Discrete strain partitioning between narrow, strike-slip dominated domains and wider, contraction dominated domains, is a common feature in oblique convergent systems (e.g., Jones and Tanner, 1995; Bowman et al., 2003). Strain partitioning of the oblique convergence involve complex systems of geologic structures. Therefore, it causes spatial and temporal redistribution of stress and strain fields over and along the part of the deforming plate and or pre-existing faults. Several previous works suggest that such strain partitioning take place once a major strike-slip fault is formed, which only occurs after a minimum of strain is accumulated (e.g., Braun and Beaumont, 1995; Burbidge and Braun, 1998; McClay et al., 2004; Leever et al., 2011). It is noteworthy that these analogue and numerical models normally generate a transpressional wedge above a velocity discontinuity at the bottom of the model. This would correspond to natural oblique convergence acting on layered sequences with no previous structures. In these situations, the strike-slip fault that triggers strain partitioning forms during strain accumulation. However, reactivation of inherited structures is a very common situation in nature (e.g., Holdsworth et al., 2001; Tavarnelli et al., 2004). In this model, this is simulated by two pre-existing faults (faults 1 and 2). The activity of slip along these major rheological steep planar boundaries favors the early nucleation of boundary-parallel deformation zones where simple shear concentrates. Consequently, strike-slip dominated, narrow transpressional zones nucleate related to these faults at the very onset of deformation. Therefore, strain partitioning is active from early deformation stages, even in low oblique, contractional dominated systems (e.g., Barcos et al., 2016).

Observations from this and previous models allow us to discuss how the main characteristics of the nucleating structure control the shape of the resulting transpressional zone. Transpressional wedges formed spontaneously above a basement fault typically present slightly asymmetric, doubly-verging geometries with a main strike-slip fault in the center (e.g., Braun and Beaumont, 1995; Burbidge and Braun, 1998; Casas et al., 2001; Leever et al., 2011). By contrast, when inherited, parallel, strongly dipping faults nucleate deformation, tabular transpressional zones are formed between them. In these cases, the rheology of the deforming medium is relevant. If the bounding blocks related by the two parallel faults show significant rheological differences with the tabular zone, narrow, strike-slip dominated zones form at these boundaries (e.g., the Torcal Shear Zone, Díaz-Azpiroz et al., 2014; Barcos et al., 2016). In our model there is no such rheological difference, thus the blocks bounded by the inherited faults do not act as rigid backstops. This permits progressive deformation to propagate outwards from the seminal tabular zone generating a transpressional wedge (Fig. 6). However, in this case, the wedge is strongly asymmetric, with very little deformation affecting the block located ahead the tabular zone (block 1) (Figs. 3, 4 and 6). It shows a single, narrow, strike-slip dominated zone located at the boundary with a semi-rigid domain, and a wide wedge with distributed, contraction dominated deformation, whose structures verge away from the strike-slip dominated zone (Figs. 3, 4 and 6). Deformation within this domain is homogeneously distributed at early deformation stages and becomes more evident with the later appearance of predominantly shortening structures (Fig. 6). These results illustrate strain partitioning in pure shear-dominated transpression is strong. However, with increasing heterogeneity of the deforming sequence, strain partitioning are expected to deviate from kinematic predictions (Jiang and Bentley, 2012; Carreras et al., 2013). Furthermore, increasing convergence, which is associated with a nonlinear increase of shear strain along the model length, can lead to thrust nappes and fold nappes (e.g., von Tscharner et al., 2016; Nabavi et al., 2017b). A similar

structural pattern is observed in northwestern part of the Zagros fold-and-thrust belt (e.g., Authemayou et al., 2006), where the dextral Main Recent Fault (MRF) splits in two subparallel, strongly dipping planes defining a parallel zone, would correspond to our faults 1 and 2 and the tabular zone in between; the Simply Folded Belt (or foreland fold-and-thrust belt, SW verging, towards the displacement) would be represented by our block 1 and the zone to the NE of the MRF (or hinterland fold-and-thrust belt) would be a domain with large deformation akin to our block 3.

However, the structures developed in natural examples (e.g., Barcos et al., 2011, 2015; Díaz-Azpiroz et al., 2014; Barcos, 2015, Nabavi et al., 2017b, Alonso-Henar et al., 2020), analogue models (e.g., Casas et al., 2001; Leever et al., 2011; Barcos et al., 2016; Crespo-Blanc et al., 2018; Fedorik et al., 2019), and the presented FE-model of inclined transpression zones, such as positive flower-like structures, brittle-ductile shear zones that generate meso-scale S-C-like structures, inclined strain fabrics (tectonic foliation and tectonic lineation), non-cylindrical folds, normal fault zones, and oblique-reverse faults, show an overall heterogeneity distributed within the area. Hence, we understand that strain partitioning develop during the evolution process of deformation under oblique convergence.

Strain paths and deformation styles have been suggested to follow non-linear paths in transpression and transtension (Fossen et al., 2019), which can be enhanced by the presence of mechanical heterogeneties. These heterogeneities are simulated in our FE-model by the presence of mechanical stratigraphy, and two inclined faults that correspond to two planar velocity discontinuities of the model set-up. The block 1 is represented in many analytical and analogue models (fixed backstop). These boundary conditions are interpreted as pre-existing planar steep structures that play a main role in both the localisation of the transpression zone and its strong strain partitioning (Tavarnelli et al., 2004; Barcos et al., 2016). In general, the bulk mechanical strength of a layered model plays a prominent role in influencing the overall

strain localisation. In this study, the model made up of an incompetent layer between two competent layers, hence, the refraction of the strains across the layer interface increases with increasing competence contrast and suggests that different sets of linking faults could develop at different structural depths (Fig. 6) (e.g., Druguet et al., 2009). The activity of slip along these major rheological steep planar boundaries favours the early nucleation of boundary-parallel deformation zones where simple shear concentrates. For high values of obliquity (convergence angles of 4-30° based on Leever et al., 2011), the long-term kinematic evolution of transpression zones can be divided into three distinct stages: indeed, an initial 'distributed strain' stage, then an 'oblique wedge' stage, and finally a 'strain partitioning' stage. An interesting result, regarding possible comparison with analytical and analogue models, is that although there is no such a rigid backstop in the model and many researches consider the fixed backstop to be completely rigid, deformation in block 1 (more often by gentle folding; and may be with some possible extensional faults, so that extensional faulting can be associated with oblique convergence) (Figs. 3 and 4) is significantly lower than in the other two, so a semi-rigid behaviour could be considered.

4.3. Kinematics and extrusion of the transpressive zone

According to the orientation of particle paths (20-30°) with respect to the transpression zone boundaries, the kinematic vorticity number (W_k) of the entire model can be estimated to be 0.4-0.65 (Fig. 9a). Furthermore, according to the displacement partitioning (Fig. 8), it can be hypothesized that the angle between the extrusion direction and the dip of the transpression zone (angle ν in Fernández and Díaz-Azpiroz, 2009) locally deviates from 0° (ν≠0°) along the dextral-reverse fault boundary. In this sense, variations in the amount of vertical extrusion from point to point along the transpression zone suggest that ν can reach up to ~18°. In addition, the angle between oblique simple shearing direction and the strike of the transpression zone (ϕ in Lin et al., 1998) is ~10° (Fig. 9b). Hence, the angle between the simple shearing and the

extrusion directions (angle ζ of Fernández and Díaz-Azpiroz, 2009) is below 90° (~82°). The shape of the strain ellipsoid in transpressional deformation strongly depends on W_k and angle ζ (Fernández and Díaz-Azpiroz, 2009). Accordingly, the values of these two parameters deduced from our results (ζ > 40° and W_k = 0.4 – 0.65) would theoretically produce, strain ellipsoids that clearly deviate from the plane-strain line, and plot in well within the flattening field of the Flinn diagram. In addition, non-parallelism between displacement vectors and the faults limiting the blocks (Fig. 8b, c), evidencing shortening and lengthening along the Y- and X-axis, respectively, also suggests that flattening took place in the deforming blocks. Therefore, the results of the FE-model plot on the triclinic transpression area (pure-shear dominated domain) of the strain triangle (Fig. 9b).

The relative obliquity of the simple shear component creates amplification (corresponding to the fold growth in the vertical or Z-direction; Frehner, 2014, 2016) and elongation (correspond to the fold growth in X-direction or parallel to fold axis; Frehner, 2014, 2016) of non-cylindrical antiforms and the system of obliquely plunging lineations. A similar inclined extrusion is also observed along the transpression zone in the Barcos et al. (2016) analogue model, and in the form of parabolic and bell-shaped velocity profile, respectively, in Newtonian and non-Newtonian materials (e.g., Mukherjee and Koyi, 2010; Mukherjee et al., 2012; Mukherjee, 2013). These findings show that the transpression zone has an important role on extrusion kinematics and velocity (e.g., Marques et al., 2018a, 2018b).

According to the FE-modelling results (Fig. 3), deformation is distributed upward toward the Earth's surface and across a zone that is kilometres wide, progressively narrowing with depth. In general, FE-modelling results show that the contraction deformation is widely distributed developing brittle and ductile structures and due to the flow of the underlying plastic layer, therefore, the model can be considered as a case of 'distributed transpression' (Schreurs and Colletta, 1998, 2002; Sançar et al., 2015). Distributed deformation in oblique tectonic

settings has been described in many studies over wide and complex zones ranging in scale from several hundred kilometres to several meters, with complex displacements, strain patterns, and rotational deformation (Molnar and Tapponier, 1975; McKenzie and Jackson, 1986; England, 1989; Schreurs and Colletta, 1998, 2002; Schreurs, 2003; Sançar et al., 2015). The results of our FE-model suggest that high-angle oblique-reverse faults can suffer a significant slip component, in addition to the amount of oblique convergence, if they are weak enough, which is related to the angle and coefficient of sliding friction, and fluid pressure. In experimental models, it can be done by the presence of a thin film of silicone putty along the pre-existing faults (e.g., Marques and Nogueira, 2008).

6. Conclusions

Combination of mechanical, geometrical, analytical and analogue models can provide a more accurate representation of inclined transpression zones and clarify some topics of this important issue. Natural examples of oblique convergence setting in transpression zones are inherently 3D and show inclined boundaries; hence, the evolution of inclined transpression zones is studied using 3D inelastic numerical finite-element modelling by applying a general triclinic inclined transpression model. In addition, use of inelastic constitutive relationships allows permanent strains to develop in response to the applied loads.

1) FE-modelling results demonstrate oblique convergence at the model was accommodated by discrete deformation at the main pre-existing inclined faults and by distributed brittle-ductile deformation at active blocks.

2) Oblique contraction at the active blocks resulted mainly in layer-parallel shortening, orthogonal to model outer boundaries, and lengthening in the horizontal and vertical directions, respectively accommodated via layer-parallel extension and up-dip extrusion. Lateral extrusion should have compensated the rest and/or volume loss took place.

3) Folding and thickening of the mobile backstop produced a non-cylindrical, asymmetric, bi-vergent anticline with permanent strains developed principally in the steep forelimb. Secondary, conjugate fault zones also accommodate oblique slip and contribute to uplift.

4) Displacement vectors (or particle paths in the XY horizontal plane) within transpressional zone are rotated counter-clockwise (ca. 20°-30°) with respect to vectors in the fixed sector. Areas with higher rotation values seem to correlate with those showing higher ellipticity values of the finite strain ellipsoids.

5) Inherited structures localise strike-slip motion, thus triggering strain partitioning from early deformation stages. A tabular transpression zone forms between pre-existing faults, while deformation propagates mainly towards the mobile block. The resulting transpression wedge can be compared to some strongly asymmetric wedges nucleated at major faults under oblique convergence conditions.

6) In general, factor like the width of the transpressional zone, the dip of boundaries, the angle of oblique convergence, mechanical stratigraphy, amount of oblique convergence, and the presence of tectonic inheritance play important roles in strain localisation, the amount of localisation along the transpression zone (decreasing with increasing obliquity), and control along- and across-strike variation in the oblique convergence settings. Even if deformation is localised along a mobile backstop and the transpression zone, parts of the study model remain undeformed at the external areas, particularly at the fixed backstop.

Acknowledgments

Seyed Tohid Nabavi thanks Prof. Jordi Carreras and Dr. Elena Druguet for their help, and constructive discussions on progressive deformation, shear zones, and transpressive settings during scientific field trips in the Cap de Creus, the Roses and the Axial Zone of Pyrenees during his research visit period in Spain. Moreover, Seyed Tohid Nabavi thanks Dr. Jonas B. Ruh for teaching and discussions on the finite difference method programming during his research visit period in the Institute of Earth Sciences "Jaume Almera" (CSIC-ICTJA), Barcelona, Spain. This work forms part of the Ph.D. thesis of Seyed Tohid Nabavi at Shahid Beheshti University, Tehran, Iran. We thank reviewers Prof. Fernando O. Marques and Prof. Soumyajit Mukherjee for constructive reviews, comments and helpful suggestions which allowed us to improve the original manuscript. Editorial and handling efforts by Prof. Ian Alsop are also gratefully acknowledged.

References

Alonso-Henar, J., Fernández, C., Martínez-Díaz, J.J., 2020. Application of the analytic model of general triclinic transpression with oblique extrusion to an active deformation zone: The Alhama de Murcia Fault (SE Iberian Peninsula). Journal of Structural Geology 130, https://doi.org/10.1016/j.jsg.2019.103924.

Alsop, G.I., Bryson, R., Hutton, D.H.W., 1998. Ductile transpression and localization of deformation along tectonic boundaries in the Caledonides of northwestern Ireland. Geological Magazine 135, 699-718.

Balgord, E.A., Carrapa, B., 2016. Basin evolution of Upper Cretaceous-Lower Cenozoic strata in the Malargüe fold-and-thrust belt: northern Neuquén Basin, Argentina. Basin Research 28, 183-206.

637 Barcos, L., 2015. Combined analytical and analogue modelling of strongly partitioned
638 transpression. The Torcal Shear Zone (external Betics). Ph.D. thesis, Universidad Pablo de
639 Olavide, Sevilla, Spain.

640 Barcos, L., Díaz-Azpiroz, M., Expósito, I., 2011. Dominios estructurales y reparto de la
641 deformación en zonas transpresivas de corteza superior (Torca de Antequera, Cadena Bética).
642 Geogaceta 50, 31-34.

643 Barcos, L., Balanyá, J.C., Díaz-Azpiroz, M., Expósito, I., Jiménez-Bonilla, A., 2015.
644 Kinematic of the Torcal Shear Zone: Transpressional tectonics in a salient-recess transition at
645 the northern Gibraltar Arc. Tectonophysics 663, 62-77.

646 Barcos, L., Díaz-Azpiroz, M., Balanyá, J.C., Expósito, I., Jiménez-Bonilla, A., Faccenna, C.,
647 2016. Analogue modelling of inclined, brittle-ductile transpression: Testing analytical models
648 through natural shear zones (external Betics). Tectonophysics 682, 169-185.

649 Bergh, S.G., Sylvester, A.G., Damte, A., Indrevær, K., 2019. Polyphase kinematic history of
650 transpression along the Mecca Hill segment of the San Andreas fault, southern California.
651 Geosphere 15, 901-934.

652 Bieniawski, Z.T., 1984. Rock Mechanics Design in Mining and Tunneling. Boston, A.A.
653 Balkema.

654 Boersma, Q.D., Douma, L.A.N.R., Bertotti, G., Barnhoorn, A., 2020. Mechanical controls on
655 horizontal stresses and fracture behavior in layered rocks: A numerical sensitivity analysis.
656 Journal of Structural Geology 130, https://doi.org/10.1016/j.jsg.2019.103907.

657

658

Bose, N., Mukherjee, S., 2019. Field documentation and genesis of back-structures in ductile and brittle regimes from the foreland part of a collisional orogen: examples from the Darjeeling-Sikkim Lesser Himalaya, India. International Journal of Earth Sciences 108, 1333-1350.

Bose, N., Dutta, D., Mukherjee, S., 2018. Role of grain-size in phyllonitisation: Insights from mineralogy, microstructures, strain analysis and numerical modeling. Journal of Structural Geology 112, 39-52.

Bott, M.H.P., 1959. The mechanics of oblique slip faulting. Geological Magazine 96, 109-117.

Bourne, S., 2003. Contrast of elastic properties between rock layers as a mechanism for the initiation and orientation of tensile failure under uniform remote compression. Journal of Geophysical Research 108, 2395, doi:10.1029/2001JB001725.

Bowman, D., King, G., Tapponnier, P., 2003. Slip partitioning by elastoplastic propagation of oblique slip at depth. Science 300, 1121-1123.

Bradley, K.E., Feng, L., Hill, E.M., Natawidjaja, D.H., Sieh, K., 2017. Implications of the diffuse deformation of the Indian Ocean lithosphere for slip partitioning of oblique plate convergence in Sumatra. Journal of Geophysical Research: Solid Earth 122, 572-591.

Brandes, C., Tanner, D.C., 2014. Fault-related folding: A review of kinematic models and their application. Earth-Sciences Review 138, 352-370.

Braun, J., Beaumont, C., 1995. Three dimensional numerical experiments of strain partitioning at oblique plate boundaries: implications for contrasting tectonic styles in the southern Coast Ranges, California, and central South Island, New Zealand. Journal of Geophysical Research 100, 18059-18074.

Burbidge, D.R., Braun, J., 1998. Analogue models of obliquely convergent continental plate boundaries. Journal of Geophysical Research 103, 15221-15237.

Burberry, C.M., 2015. Spatial and temporal variation in penetrative strain during compression: Insights from analog models. Lithosphere 7, 611-624.

Calignano, E., Sokoutis, D., Willingshofer, E., Brun, J.-P., Gueydan, F., Cloetingh, S., 2017. Oblique contractional reactivation of inherited heterogeneities: Cause for arcuate orogens. Tectonics 36, 542-558.

Carmichael, R.S., 1982. Handbook of Physical Properties of Rocks, vol. 2. Chemical Rubber Company Press, Boca Raton, Florida.

Carreras, J., Cosgrove, J.W., Druguet, E., 2013. Strain partitioning in banded and/or anisotropic rocks: Implications for inferring tectonic regimes. Journal of Structural Geology 50, 7-21.

Carreras, J., Druguet, E., 2019. Complex fold patterns developed by progressive deformation. Journal of Structural Geology 125, 195-201.

Casas, A.M., Gapais, D., Naplas, T., Besnard, K., Román-Berdiel, T., 2001. Analogue models of transpressive systems. Journal of Structural Geology 23, 733-743.

Cooke, M., Underwood, C., 2001. Fracture termination and step-over at bedding interfaces due to frictional slip and interface opening. Journal of Structural Geology 23, 223-238.

Crespo-Blanc, A., Jiménez-Bonilla, A., Balanyá, J.C., Expósito, I., Díaz-Azpiroz, M., 2018. From field data to lithospheric-scale models going through analogue experiments: the Gibraltar Arc system revisited in the light of the external zones structural evolution. Revista de la Sociedad Geológica de España 31, 111-122.

Cruz, L., Teyssier, C., Perg, L., Take, A., Fayon, A., 2008. Deformation, exhumation, and topography of experimental doubly-vergent orogenic wedges subjected to asymmetric erosion. Journal of Structural Geology 30, 98-115.

Curtis, M.L., 1998. Development of kinematic partitioning within a pure-shear dominated dextral transpression zone: the southern Ellsworth Mountains, Antarctica. In: Holdsworth, R.E., Strachan, R.A., Dewey, J.F. (Eds.), Continental Transpressional and Transtensional Tectonics, Geological Society of London, Special Publications 135, pp. 289-306.

Czeck, D.M., Hudleston, P.J., 2003. Testing models for obliquely plunging lineations in transpression: a natural example and theoretical discussion. Journal of Structural Geology 25, 959-982.

Czeck, D.M., Hudleston, P.J., 2004. Physical experiments of vertical transpression with localized nonvertical extrusion. Journal of Structural Geology 26, 573-581.

Dasgupta, S., Mandal, N., Bose, S., 2015. How far does a ductile shear zone permit transpression? In: Mukherjee, S., Mulchrone, K.F. (Eds.), Ductile Shear Zones: From Micro- to Macro-scales. Springer, p. 14-29.

Davis, J.R., Titus, S.J., 2011. Homogenous steady deformation: A review of computational techniques. Journal of Structural Geology 33, 1046-1062.

Davis, J.R., Titus, S.J., Horsman, E., 2013. Non-steady homogeneous deformations: Computational techniques using Lie theory, and application to ellipsoidal markers in naturally deformed rocks. Journal of Structural Geology 56, 142-155.

Derikvand, B., Alavi, S.A., Abdollahie Fard, I., Hajialibeigi, H., 2018. Folding style of the Dezful Embayment of Zagros Belt: Signature of detachment horizons, deep-rooted faulting and syn-deformation deposition. Marine and Petroleum Geology 91, 501-518.

725 Dewey, J.F., Holdsworth, R.E., Strachan, R.A., 1998. Transpression and transtension zones.
726 In: Holdsworth, R.E., Strachan, R.A., Dewey, J.F. (Eds.), Continental Transpressional and
727 Transtensional Tectonics. Geological Society of London, Special Publications 135, pp. 1-14.

728 Díaz-Azpiroz, M., Fernández, C., 2005. Kinematic analysis of the southern Iberian shear zone
729 and tectonic evolution of the Acebuches metabasites (SW Variscan Iberian Massif). Tectonics
730 24(3), doi:10.1029/2004TC001682.

731 Díaz-Azpiroz, M., Barcos, L., Balanyá, J.C., Fernández, C., Expósito, I., and Czeck, D.M.,
732 2014. Applying a general triclinic transpression model to highly partitioned brittle-ductile shear
733 zones: A case study from the Torcal de Antequera massif, external Betics, southern Spain.
734 Journal of Structural Geology 68, 316-336.

735 Díaz-Azpiroz, M., Brune, S., Leever, K.A., Fernández, C., Czeck, D.M., 2016. Tectonics of
736 oblique plate boundary systems. Tectonophysics 693, 165-170.

737 Díaz-Azpiroz, M., Fernández, C., Czeck, D.M., 2019. Are we studying deformed rocks in the
738 right sections? Best practices in the kinematic analysis of 3D deformation zones. Journal of
739 Structural Geology 125, 218-225.

740 Druguet, E., Alsop, G.I., Carreras, J., 2009. Coeval brittle and ductile structures associated with
741 extreme deformation partitioning in a multilayer sequence. Journal of Structural Geology 31,
742 498-511.

743 England, P., 1989. Large rates of rotation in continental lithosphere undergoing distributed
744 deformation. In: Kissel, C., Laj, C. (Eds.), Paleomagnetic Rotation and Continental
745 Deformation. Kluwer, Dordrecht, 157-164.

746 Eschbac, O.W., 1961. Handbook of Engineering Fundamentals, Handbook Series. John Wiley
747 and Sons, New York.

748 Fedorik, J., Zwaan, F., Schreurs, G., Toscani, G., Bonini, L., Seno, S., 2019. The interaction
749 between strike-slip dominated fault zones and thrust belt structures: Insights from 4D analogue
750 models. Journal of Structural Geology 122, 89-105.

751 Fernández, C., Díaz-Azpiroz, M., 2009. Triclinic transpression zones with inclined extrusion.
752 Journal of Structural Geology 31, 1255-1269.

753 Fernández, C., Czeck, D.M., Díaz-Azpiroz, M., 2013. Testing the model of oblique
754 transpression with oblique extrusion in two natural cases: Steps and consequences. Journal of
755 Structural Geology 54, 85-102.

756 Ferrill, D.A., Morris, A.P., 2008. Fault zone deformation controlled by carbonate mechanical
757 stratigraphy, Balcones fault system, Texas. American Association of Petroleum Geologists
758 Bulletin 92, 359-380.

759 Ferrill, D.A., Morris, A.P., McGinnis, R.N., Smart, K.J., Wigginton, S.S., Hill, N.J., 2017.
760 Mechanical stratigraphy and normal faulting. Journal of Structural Geology 94, 275-302.

761 Fossen, H., Tikoff, B., 1993. The deformation matrix for simultaneous simple shearing, pure
762 shearing and volume change, and its application to transpression-transtension tectonics. Journal
763 of Structural Geology 15, 413-422.

764 Fossen, H., Tikoff, B., Teyssier, C., 1994. Strain modelling of transpressional and
765 transtensional deformation. Norsk Geologisk Tidsskrift 74, 134-145.

766 Fossen, H., Tikoff, B., 1998. Extended models of transpression and transtension, and
767 application to tectonic settings. In: Holdsworth, R.E., Strachan, R.A., Dewey, J.F. (Eds.),
768 Continental Transpressional and Transtensional Tectonics, Geological Society of London,
769 Special Publications 135, pp. 15-33.

770 Fossen, H., Teyssier, C., Whitney, D.L., 2013. Transtensional folding. Journal of Structural
771 Geology 56, 89-102.

772 Fossen, H., Cavalcante, G.C.G., 2017. Shear zones – A review. Earth-Science Reviews 171,
773 434-455.

774 Fossen, H., Cavalcante, G.C.G., Pinheiro, R.V.L., Archanjo, C.J., 2019. Deformation –
775 Progressive or multiphase? Journal of Structural Geology 125, 82-99.

776 Frehner, M., 2014. 3D fold growth rates. Terra Nova 26, 417-424.

777 Frehner, M., 2016. 3D fold growth in transpression. Tectononphysics 693, 183-196.

778 Ghosh, N., Chakra, M., Chattopadhyay, A., 2014. An experimental approach to strain pattern
779 and folding in unconfined and/or partitioned transpressional deformation. International Journal
780 of Earth Sciences 103, 349-365.

781 Graveleau, F., Malavieille, J., Dominguez, S., 2012. Experimental modelling of orogenic
782 wedges: A review. Tectonophysics 538-540, 1-66.

783 Harland, W.B., 1971. Tectonic transpression in Caledonian Spitsbergen. Geological Magazine
784 108, 27-42.

785 Holdsworth, R.E., Stewart, M., Imber, J., Strachan, R.A., 2001. The structure and rheological
786 evolution of reactivated continental fault zones: A review and case study. In: Miller, J.A.,
787 Holdsworth, R.E., Buick, I.S., Hand, M. (Eds.), Continental Reactivation and Reworking.
788 Geological Society of London, Special Publications 184, p. 115-137.

789 Horsman, E., Tikoff, B., Czeck, D., 2008. Rheological implications of heterogeneous
790 deformation at multiple scales in the Late Cretaceous Sierra Nevada, California. Geological
791 Society of America Bulletin 120, 238-255.

792 Hudleston, P.J., Schultz-Ela, D., Southwick, D.L., 1988. Transpression in an Archean
793 greenstone belt, northern Minnesota. Canadian Journal of Earth Sciences 25, 1060-1068.

794 Hughes, A.N., Benesh, N.P., Shaw, J.H., 2014. Factors that control the development of fault-
795 bend versus fault-propagation folds: Insights from mechanical models based on the discrete
796 element method (DEM). Journal of Structural Geology 68, 121-141.

797 Hughes, A.N., Shaw, J.H., 2015. Insights into the mechanics of fault-propagation folding
798 styles. Geological Society of America Bulletin 127(11-12), 1752-1765.

799 Iacopini, D., Passchier, C.W., Koehn, D., Carosi, R., 2007. Fabric attractors in general triclinic
800 glow systems and their application to high strain shear zones: A dynamical systems approach.
801 Journal of Structural Geology 29, 298-317.

802 Jaeger, J.C., Cook, N.G.W., Zimmerman, R.W., 2007. Fundamental of Rock Mechanics. 4th
803 edition, Blackwell, Malden.

804 Jiang, D., 2007. Sustainable transpression: an examination of strain and kinematics in
805 deforming zones with migrating boundaries. Journal of Structural Geology 29, 1984-2005.

806 Jiang, D., Bentley, C., 2012. A micromechanical approach for simulating multiscale fabrics in
807 large-scale high-strain zones: Theory and application. Journal of Geophysical Research 117,
808 doi:10.1029/2012JB009327.

809 Jones, R.R., Tanner, P.W.G., 1995. Strain partitioning in transpression zones. Journal of
810 Structural Geology 17, 793-802.

811 Jones, R.R., Holdsworth, R.E., Clegg, P., McCaffrey, K., Tavarnelli, E., 2004. Inclined
812 transpression. Journal of Structural Geology 26, 1531-1548.

Jones, R.R., Holdsworth, R.E., McCaffrey, K., Clegg, P., Tavarnelli, E., 2005. Scale dependence, strain compatibility and heterogeneity of three-dimensional deformation during mountain building: a discussion. Journal of Structural Geology 27, 1190-1204.

Koyi, H.A., Maillot, B., 2007. Tectonic thickening of hanging-wall units over a ramp. Journal of Structural Geology 29, 924-932.

Leever, K.A., Gabrielsen, R.H., Sokoutis, D., Willingshofer, E., 2011. The effect of convergence angle on the kinematic evolution of strain partitioning in transpressional brittle wedges: Insights from analog modeling and high-resolution digital image analysis. Tectonics 30, TC2013, doi:10.1029/2010TC002823.

Li, Z., Zhang, P., Zheng, W., Jia, D., Hubbard, J., Almeida, R., Sun, C., Shi, X., Li, T., 2018. Oblique thrusting and strain partitioning in the Longmen Shan fold-and-thrust belt, eastern Tibetan Plateau. Journal of Geophysical Research: Solid Earth 123, 4431-4453.

Lin, S., Jiang, D., Williams, P.F., 1998. Transpression (or transtension) zones of triclinic symmetry; natural example and theoretical modelling. In: Holdsworth, R.E., Strachan, R.A., Dewey, J.F. (Eds.), Continental Transpressional and Transtensional Tectonics, Geological Society of London, Special Publications 135, pp. 41-57.

Malz, A., Madritsch, H., Meier, B., Kley, J., 2016. An unusual triangle zone in the external northern Alpine foreland (Switzerland): Structural inheritance, kinematics and implications for the development of the adjacent Jura fold-and-thrust belt. Tectonophysics 670, 127-143.

Marques, F.O., Nogueira, C.R., 2008. Normal fault inversion by orthogonal compression: Sandbox experiments with weak faults. Journal of Structural Geology 30, 761-766.

Marques, F.O., Ranalli, G., Mandal, N., 2018a. Tectonic overpressure at shallow depth in the lithosphere: The effects of boundary conditions. Tectonophysics 746, 702-715.

836 Marques, F.O., Mandal, N., Ghosh, S., Ranalli, G., Bose, S., 2018b. Channel flow, tectonic
837 overpressure, and exhumation of high-pressure rocks in the Greater Himalayas. Solid Earth 9,
838 1061-1078.

839 McClay, K.R., Buchanan, P.G., 1992. Thrust faults in inverted extensional basins. In: McClay,
840 K.R. (Ed.), Thrust Tectonics, pp. 93-104.

841 McClay, K.R., Whitehouse, P.S., Dooley, T., Richards, M., 2004. 3D evolution of fold and
842 thrust belts formed by oblique convergence. Marine and Petroleum Geology 21, 857-877.

843 McGinnis, R.N., Ferrill, D.A., Morris, A.P., Smart, K.J., 2016. Insight on mechanical
844 stratigraphy and subsurface interpretation. In: Krantz, B., Ormand, C., Freeman, B. (Eds.), 3-
845 D Structural Interpretation: Earth, Mind, and Machine. American Association of Petroleum
846 Geologists Memoir 111, pp. 111-120.

847 McKenzie, D., Jackson, J., 1986. A block model of distributed deformation by faulting. Journal
848 of Geological Society, London 143, 349-353.

849 Michie, E.A.H., Haines, T.J., Healy, D., Neilson, J.E., Timms, N.E., Wibberley, C.A.J., 2014.
850 Influence of carbonate facies on fault zone architecture. Journal of Structural Geology 65, 82-
851 99.

852 Molnar, P., Taponnier, P., 1975. Cenozoic tectonics of Asia: effects of a continental collision.
853 Science 198, 419-426.

854 Morris, A., Ferrill, D.A., Henderson, D.B., 1996. Slip-tendency analysis and fault reactivation.
855 Geology 24, 275-278.

856 Morris, A.P., Ferrill, D.A., McGinnis, R.N., 2016. Using fault displacement and slip tendency
857 to estimate stress states. Journal of Structural Geology 83, 60-72.

858 Mukherjee, S., 2013. Channel flow extrusion model to constrain dynamic viscosity and Prandtl
859 number of the Higher Himalayan Shear Zone. International Journal of Earth Sciences 102,
860 1811-1835.

861 Mukherjee, S., Koyi, H.A., 2010. Higher Himalayan Shear Zone, Sutlej section: structural
862 geology and extrusion mechanism by various combinations of simple shear, pure shear and
863 channel flow in shifting modes. International Journal of Earth Sciences 99, 1267-1303.

864 Mukherjee, S., Koyi, H.A., Talbot, C.J., 2012. Implication of channel flow analogue models
865 for extrusion of the Higher Himalayan Shear Zone with special reference to the out-of-sequence
866 thrusting. International Journal of Earth Sciences 101, 253-272.

867 Nabavi, S.T., Alavi, S.A., Mohammadi, S., Ghassemi, M.R., Frehner, M., 2017a. Analysis of
868 transpression within contractional fault steps using finite-element method. Journal of Structural
869 Geology 96, 1-20.

870 Nabavi, S.T., Díaz-Azpiroz, M., Talbot, C.J., 2017b. Inclined transpression in the Neka Valley,
871 eastern Alborz, Iran. International Journal of Earth Sciences 106, 1815-1840.

872 Nabavi, S.T., Rahimi-Chakdel, A., Khademi, M., 2017c. Structural pattern and emplacement
873 mechanism of the Neka Valley nappe complex, eastern Alborz, Iran. International Journal of
874 Earth Sciences 106, 2387-2405.

875 Nabavi, S.T., Alavi, S.A., Mohammadi, S., Ghassemi, M.R., 2018a. Mechanical evolution of
876 transpression zones affected by fault interactions: Insights from 3D elasto-plastic finite element
877 models. Journal of Structural Geology 106, 19-40.

878 Nabavi, S.T., Alavi, S.A., Maerten, F., 2018b. 2D finite-element elastic models of
879 transtensional pull-apart basins. Comptes Rendus Geoscience 350, 222-230.

Nabavi, S.T., Alavi, S.A., Javanbakht J., H., 2019. The Dinevar trantensional pull-apart basin, NW Zagros Mountains, Iran: a geological study and comparison to 2D finite element elastic models. International Journal of Earth Sciences 108, 329-346.

Nevitt, J.M., Pollard, D.D., Warren, J.M., 2014. Evaluation of transtension and transpression within contractional fault steps: comparing kinematic and mechanical models to field data. Journal of Structural Geology 60, 55-69.

Nevitt, J.M., Warren, J.M., Pollard, D.D., 2017. Testing constitutive equations for brittle-ductile deformation associated with faulting in granitic rock. Journal of Geophysical Research: Solid Earth 122, 6269-6293.

Nussbaum, C., Kloppenburg, A., Caër, T., Bossart, P., 2017. Tectonic evolution around the Mont Terri rock laboratory, northwestern Swiss Jura: constraints from kinematic forward modelling. Swiss Journal of Geosciences 110, 39-66.

Peacock, D.C.P., Dimmen, V., Rotevatn, A., Sanderson, D.J., 2017. A boarder classification of damage zones. Journal of Structural Geology 102, 179-192.

Philippon, M., Corti, G., 2016. Obliquity along plate boundaries. Tectonophysics 693, 171-182.

Pollard, D.D., Fletcher, R.C., 2005. Fundamental of Structural Geology. Cambridge University Press.

Powell, C.M., 1987. Inversion tectonics in S.W. Dyfed. Proceedings of the Geologists' Association 98(3), 193-203.

Ratschbacher, L., Merle, O., Davy, P., Cobbold, P.R., 1991. Lateral extrusion in the eastern Alps, Part 1: Boundary conditions and experiments scaled for gravity. Tectonics 10, 245-256.

902 Richard, P., Cobbold, P.R., 1990. Experimental insights into partitioning of fault motions in
903 continental convergent wrench zones. Annals Tectonicae 4, 35-44.

904 Robin, P.-Y.F., Cruden, A.R., 1994. Strain and vorticity patterns in ideally ductile transpression
905 zones. Journal of Structural Geology 4, 447-466.

906 Rosas, F.M., Duarte, J.C., Almeida, P., Schellart, W.P., Riel, N., Terrinha, P., 2017. Analogue
907 modelling of thrust systems: Passive vs. active hanging wall strain accommodation and sharp
908 vs. smooth fault-ramp geometries. Journal of Structural Geology 99, 45-69.

909 Ruh, J.B., Kaus, B.J.P., Burg, J.-P., 2012. Numerical investigation of deformation mechanics
910 in fold-and-thrust belts: Influence of rheology of single and multiple décollements. Tectonics
911 31, TC3005, doi:10.1029/2011TC003047.

912 Ruh, J.B., Gerya, T., Burg, J.-P., 2014. 3D effects of strain vs. velocity weakening on
913 deformation patterns in accretionary wedges. Tectonophysics 615-616, 122-141.

914 Ruh, J.B., Gerya, T., Burg, J.-P., 2017. Toward 4D modeling of orogenic belts: Example from
915 the transpressive Zagros Fold Belt. Tectonophysics 702, 82-89.

916 Sadeghi, S., Storti, F., Yassaghi, A., Nestola, Y., Cavozzi, C., 2016. Experimental deformation
917 partitioning in obliquely converging orogens with lateral variation of basal décollement
918 rheology: Influences for NW Zagros, Iran. Tectonophysics 693, 223-238.

919 Sançar, T., Zabcı, C., Akyüz, H.S., Sunal, G., Villa, I.M., 2015. Distributed transpressive
920 continental deformation: The Varto Fault Zone, eastern Turkey. Tectonophysics 661, 99-111.

921 Sanderson, D.J., Marchini, W.R.D., 1984. Transpression. Journal of Structural Geology 6, 449-
922 458.

923 Sarkarinejad, K., Godin, L., Faghih, A., 2009. Kinematic vorticity flow analysis and $^{40}Ar/^{39}Ar$
924 geochronology related to inclined extrusion of the HP-LT metamorphic rocks along the Zagros
925 accretionary prism, Iran. Journal of Structural Geology 31, 691-706.

926 Sarkarinejad, K., Razavi Pash, R., Motamedi, H., Yazdani, M., 2018. Deformation and
927 kinematic evolution of the subsurface structures: Zagros foreland fold-and-thrust belt, northern
928 Dezful Embayment, Iran. International Journal of Earth Sciences 107, 1287-1304.

929 Sarkarinejad, K., Partabian, A., Faghih, A., 2013. Variation in the kinematics of deformation
930 along the Zagros inclined transpression zone, Iran: Implications for defining a curved inclined
931 transpression zone. Journal of Structural Geology 48, 126-136.

932 Schreurs, G., 2003. Fault development and interaction in distributed strike-slip shear zones: an
933 experimental approach. In: Storti, F., Holdsworth, R.E., Salvini, F. (Eds.), Intraplate Strike-slip
934 Deformation Belts. Geological Society of London, Special Publications 210, 35-52.

935 Schreurs, G., Colletta, B., 1998. Analogue modelling of faulting in zones of continental
936 transpression and transtension. In: Holdsworth, R.E., Strachan, R.A., Dewey, J.F. (Eds.),
937 Continental Transpressional and Transtensional Tectonics, Geological Society of London,
938 Special Publications 135, pp. 59-79.

939 Schreurs, G., Colletta, B., 2002. Analogue modelling of continental transpression. In: Schellart,
940 W.P., Passchier, W.P. (Eds.), Analogue Modelling of Large-scale Tectonic Processes. Journal
941 of Virtual Explorer 7, pp. 103-114.

942 Schulmann, K., Gayer, R., 2000. A model for a continental accretionary wedge developed by
943 oblique collision: the NE Bohemian Massif. Journal of the Geological Society, London 157,
944 401-416.

945 Schulmann, K., Thompson, A.B., Lexa, O., Ježek, J., 2003. Strain distribution and fabric
946 development modeled in active and ancient transpressive zones. Journal of Geophysical
947 Research 108, ETG 6-1-ETG 6-15, doi:10.1029/2001JBooo632.

948 Simonetti, M., Carosi, R., Montomoli, C., Langone, A., D´Addario, E., Mammoliti, E., 2018.
949 Kinematic and geochronological constraints on shear deformation in the Ferriere-Mollières
950 shear zone (Argentera-Mercantour Massif, Western Alps): implications for the evolution of the
951 Southern European Variscan Belt. International Journal of Earth Sciences 107, 2163-2189.

952 Stephens, T.L., Walker, R.J., Healy, D., Bubeck, A., England, R.W., McCaffrey, K.J.W., 2017.
953 Igneous sills record far-field and near field stress interactions during volcano construction: Isle
954 of Mull, Scotland. Earth and Planetary Science Letters 478, 159-174.

955 Sullivan, W.A., Law, R.D., 2007. Deformation path partitioning within the transpressional
956 White Mountain shear zone, California and Nevada. Journal of Structural Geology 29, 583-
957 598.

958 Tavarnelli, E., Holdsworth, R.E., Clegg, P., Jones, R.R., McCaffrey, K.J.W., 2004. The
959 anatomy and evolution of a transpressional imbricate zone, Southern Uplands, Scotland.
960 Journal of Structural Geology 26, 1341-1360.

961 Tikoff, B., Teyssier, C., 1994. Strain modeling of displacement-field partitioning in
962 transpressional orogens. Journal of Structural Geology 16, 1575-1588.

963 Tikoff, B., Peterson, K., 1998. Physical experiments of transpressional folding. Journal of
964 Structural Geology 20, 661-672.

965 Titus, S.J., Housen, B., Tikoff, B., 2007. A kinematic model for the Rinconada fault system in
966 central California based on structural analysis of en echelon folds and paleomagnetism. Journal
967 of Structural Geology 29, 961-982.

968 Toy, V.G., Norris, R.J., Prior, D.J., Walrond, M., Cooper, A.F., 2013. How do lineations reflect
969 the strain history of transpressive shear zones? The example of the active Alpine Fault Zone,
970 New Zealand. Journal of Structural Geology 50, 187-198.

971 van Gelder, I.E., Willingshofer, E., Sokoutis, D., Cloetingh, S.A.P.L., 2017. The interplay
972 between subduction and lateral extrusion: A case study for the European Easter Alps based on
973 analogue models. Earth and Planetary Science Letters 472, 82-94.

974 Viola, G., Henderson, I.C., 2010. Inclined transpression at the toe of an arcuate thrust: an
975 example from the Precambrian 'Mylonite Zone' of the Sveconorwegian orogen. In: Law, R.D.,
976 Butler, R.W.H., Holdsworth, R.E., Krabbendam, M., Strachan, R.A. (Eds.), Continental
977 Tectonics and Mountain Building: The Legacy of Peach and Horne. Geological Society of
978 London, Special Publications 335, pp. 715-737.

979 Vitale, S., Mazzoli, S., 2008. Heterogeneous shear zone evolution: The role of shear strain
980 hardening/softening. Journal of Structural Geology 30, 1383-1395.

981 Vitale, S., Mazzoli, S., 2015. From finite to incremental strain: insights into heterogeneous
982 shear zone evolution. In: Mukherjee, S., Mulchrone, K.F. (Eds.), Kinematics of Ductile Shear
983 Zones in Meso- and Micro-scales. Wiley and Blackwell, pp. 3-13.

984 von Tscharner, M., Schmalholz, S.M., Epard, J.-L., 2016. 3-D numerical models of viscous
985 flow applied to fold nappes and the Rawil depression in the Helvetic nappe system (western
986 Switzerland). Journal of Structural Geology 86, 32-46.

987 Xypolias, P., Gerogiannis, N., Chatzaras, V., Papapavlou, K., Kruckenberg, S.C., Aravadinou,
988 E., Miches, Z., 2018. Using incremental elongation and shearing to unravel the kinematics of
989 a complex transpressional zone. Journal of Structural Geology 115, 64-81.

990 Xu, S., Fukuyama, E., Ben-Zion, Y., Ampuero, J.-P., 2015. Dynamic rupture activation of
991 backthrust fault branching. Tectonophysics 644-645, 161-183.

992 Zanchi, A., Zanchetta, S., Balini, M., Ghassemi, M.R., 2016. Oblique convergence during the
993 Cimmerian collision: Evidence from the Triassic Aghdarband Basin, NE Iran. Godwana
994 Research 38, 149-170.

995 Ziesch, J., Tanner, D.C., Krawczyk, C.M., 2014. Strain associated with the fault-parallel flow
996 algorithm during kinematic fault displacement. Mathematical Geoscience 46(1), 59-73.

997

998

999

1000

1001

1002

1003

1004

1005

1006

1007

1008

1009

1010

Figure captions

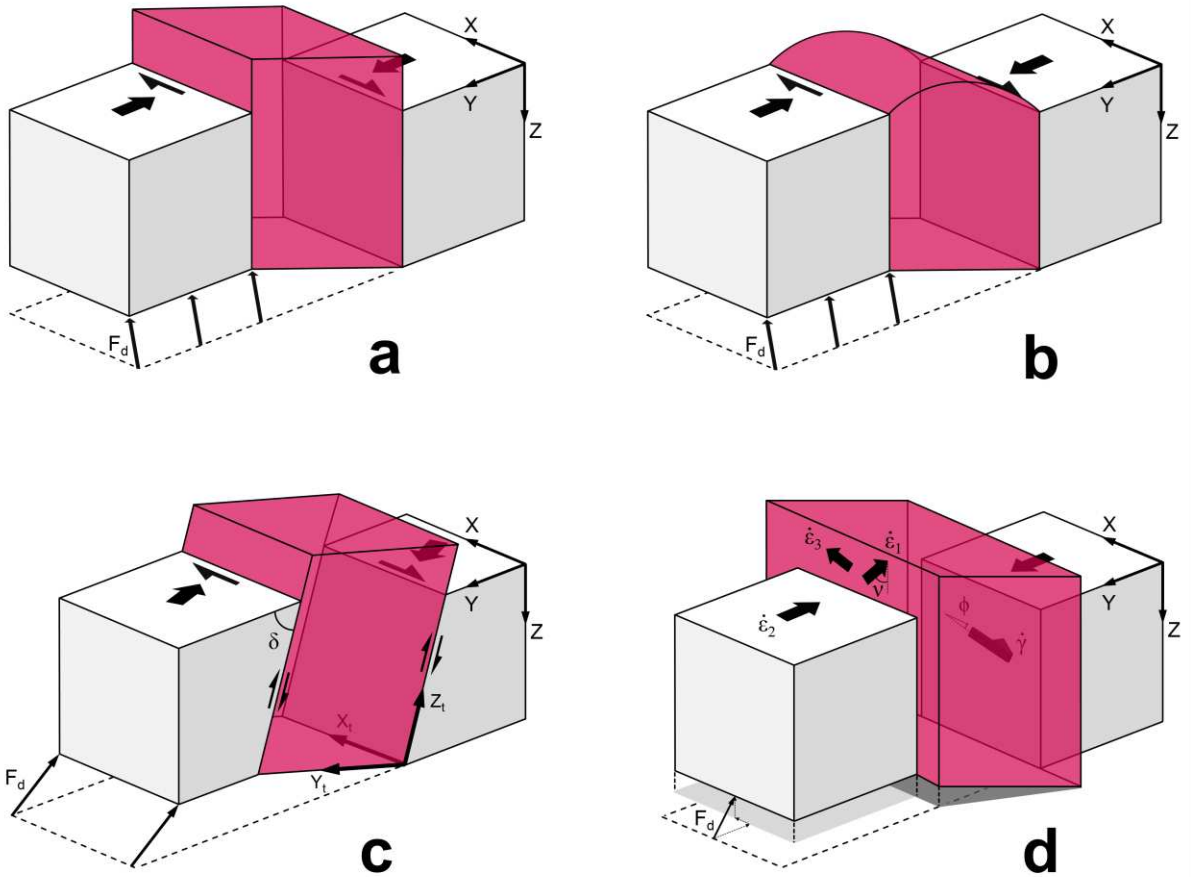

Fig. 1. Models of transpression zones mentioned in the text. Reference frame: X is horizontal and parallel to the strike of the transpression zone boundary; Y is horizontal and normal to the transpression zone boundary; and Z is vertical. F_d is the convergence vector between the zone-bounding blocks. a) Classical model of monoclinic transpression zone (Sanderson and Marchini, 1984; Fossen and Tikoff, 1993). b) Transpression zone model with no-slip boundaries (Robin and Cruden, 1994; Dutton, 1997). c) Inclined transpression kinematic model (Jones et al., 2004). The reference coordinate system, X_t, Y_t, and Z_t is fixed to the shear zone and differs from the far-field coordinate system X, Y, Z. δ is the dip of the zone boundaries. d) Model of triclinic transpression with oblique simple shear and inclined extrusion direction (Fernández and Díaz-Azpiroz, 2009). Transpression obliquity ϕ is the angle between the simple shearing direction and the strike of the transpression zone. $\dot{\gamma}$ is simple shear strain rate. $\dot{\varepsilon}_1$, $\dot{\varepsilon}_2$ and $\dot{\varepsilon}_3$ are strain rates. Extrusion obliquity ν is the angle between the extrusion direction ($\dot{\varepsilon}_1$) and the dip of the transpression zone.

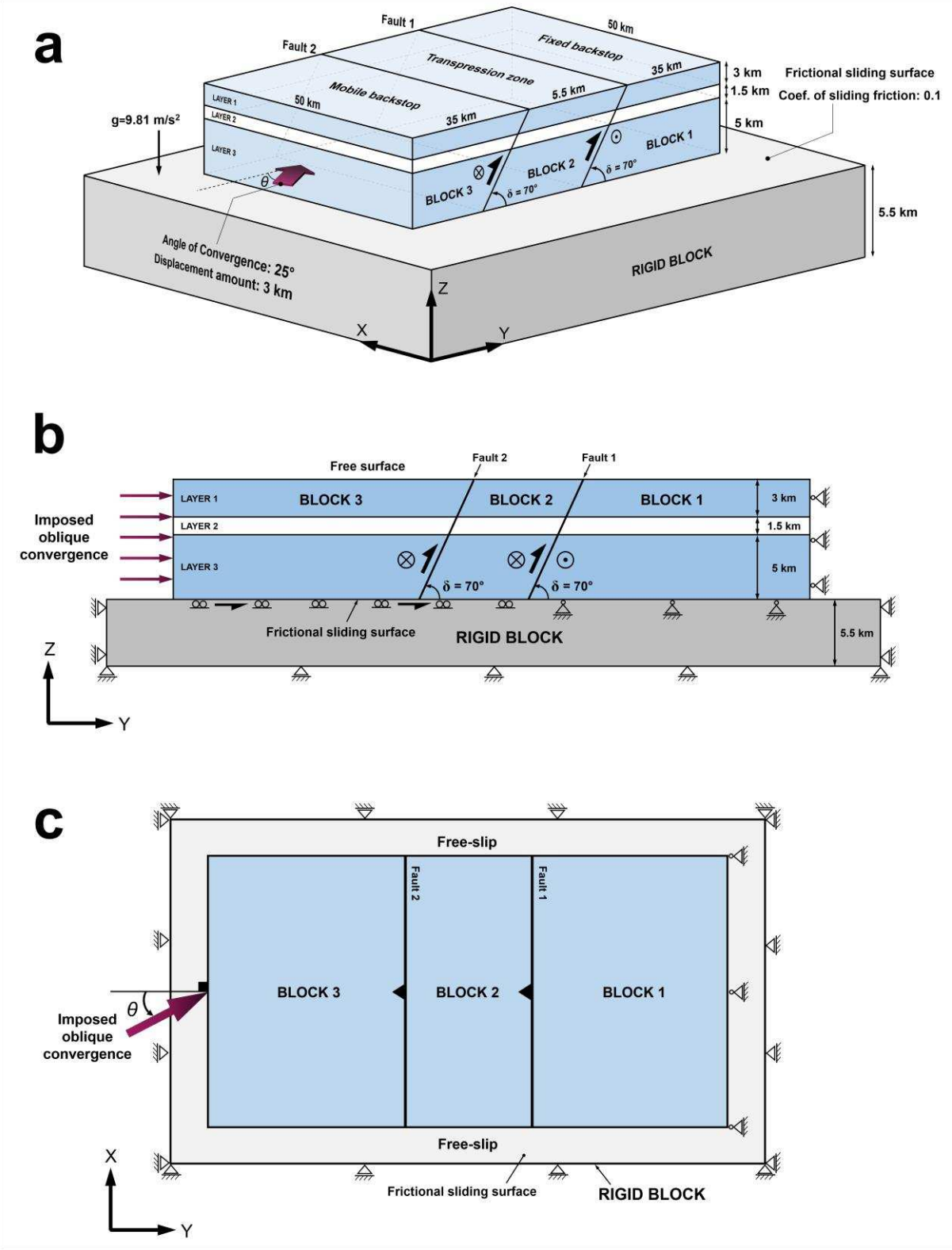

Fig. 2. Initial setup of the three-dimensional FE-model: a) Three-dimensional block diagram; b) cross-sectional view (YZ-plane); and c) map view (XY-plane) of the model showing the imposed load, boundary conditions, and rheology of mechanical layering. Boundary conditions

are no-slip at the right side and at the bottom of block 1, constant oblique convergence in the horizontal direction at the left side and at the bottom of blocks 2 and 3; and free surface at the top boundary. The free surface boundary condition at the top model face allow self-consistent evolution of topography. In addition, both lateral boundary conditions are defined as free-slip along the boundary planes. Finally, the study model is discretised to 15032 three-dimensional 8-node elements.

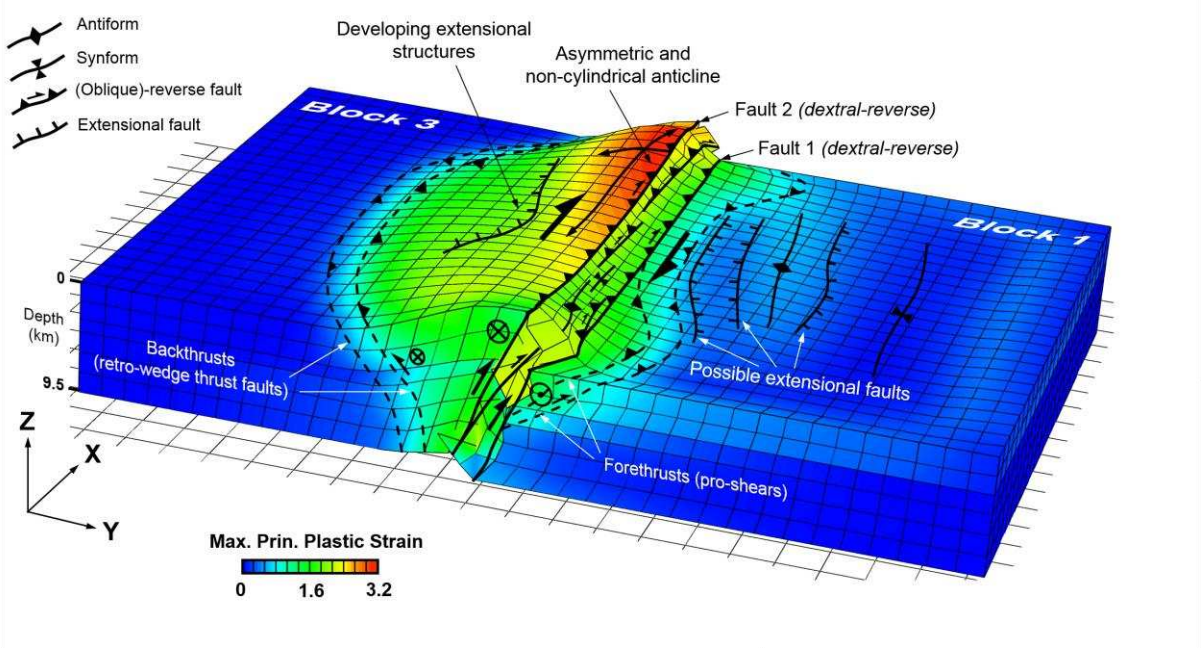

Fig. 3. Observed structural geometry, internal deformation and distribution of maximum principal plastic strain resulting from oblique convergence for a heterogeneous and anisotropic mechanical model of the inclined, brittle-ductile transpression zone. The strain values for all elements are obtained by integrating the strain rate numerically in a material frame and the maximum plastic strain is the largest positive contractional strains.

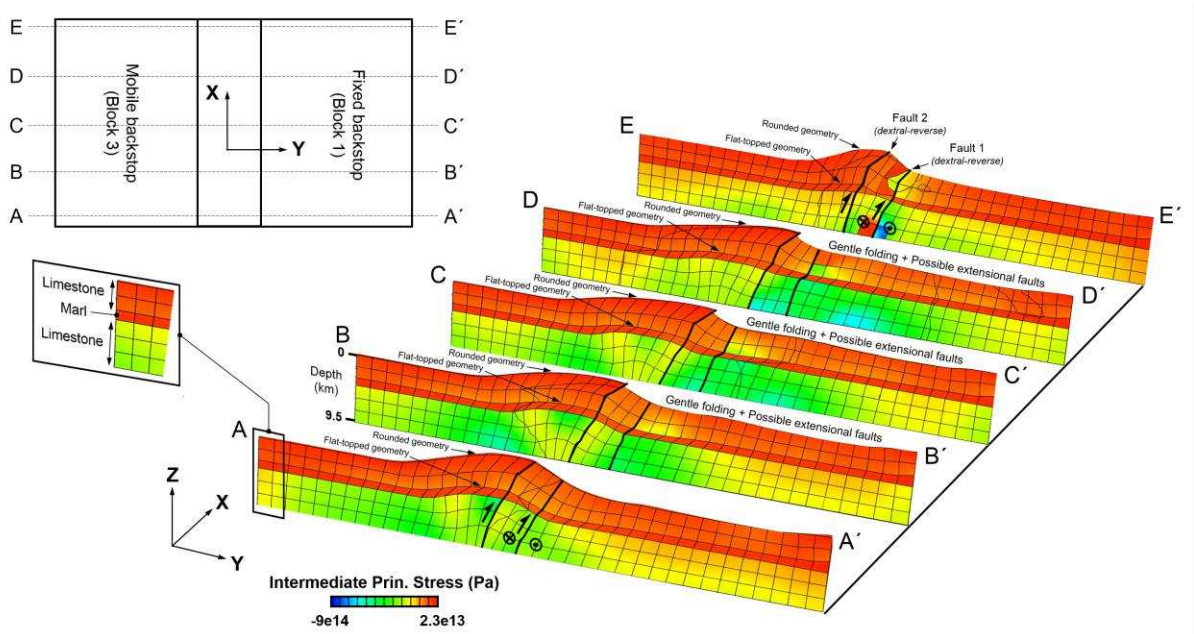

1042

1043 **Fig. 4.** Vertical cross-sections of the model with distribution of the intermediate principal stress
1044 (same colour scale for all profiles). The locations of the vertical sections are shown in the left
1045 map view. The model actually underwent a contraction and the minus sign in the stress bar
1046 scale indicates minimum values of compressive stress and auto limit calculations. When the
1047 initial conditions is considered (zero stress and strain) the recovery in elastic rheology will
1048 appear as a negative value.

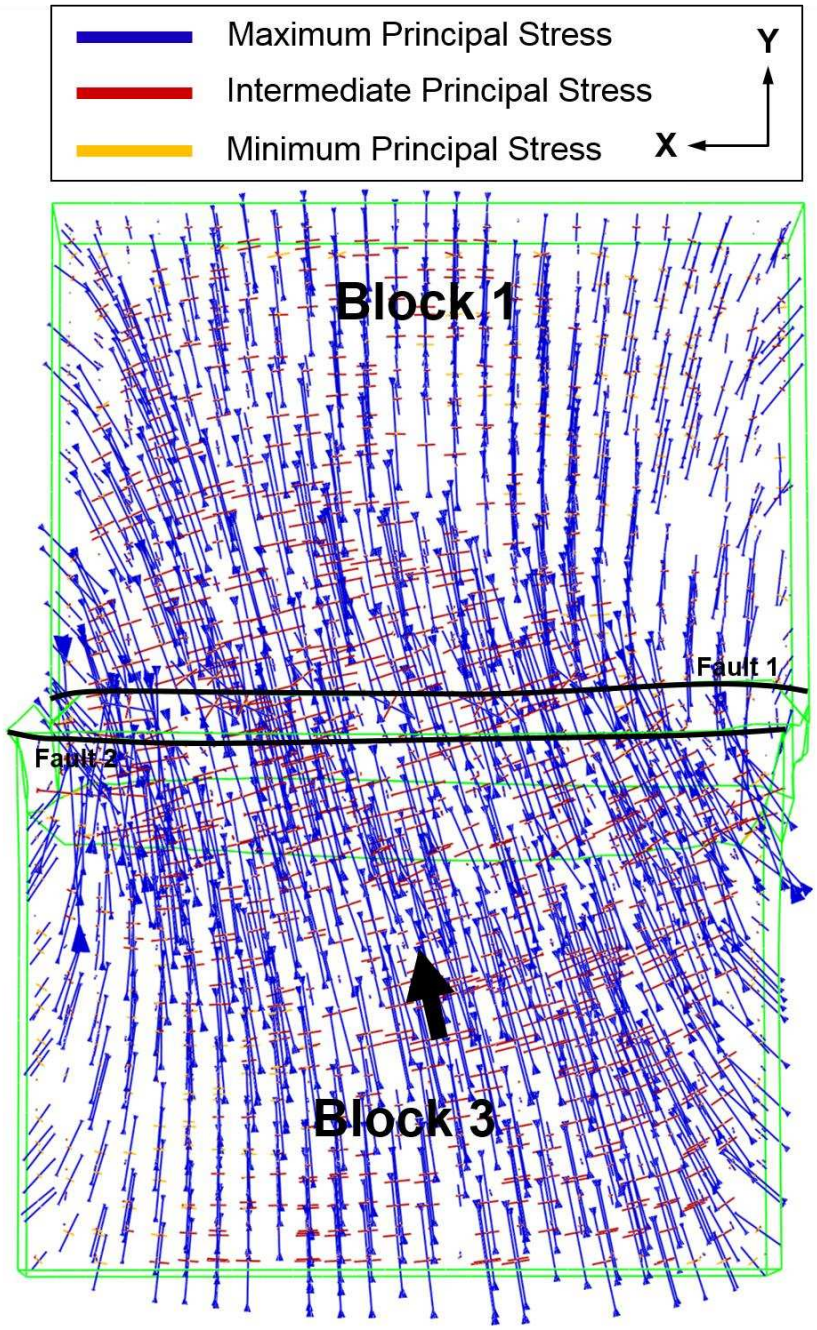

1049

1050 **Fig. 5.** Top view of FE-model results representing the spatial distribution of principal stress

1051 axes (also compare with fig. 9b in Authemayou et al., 2006).

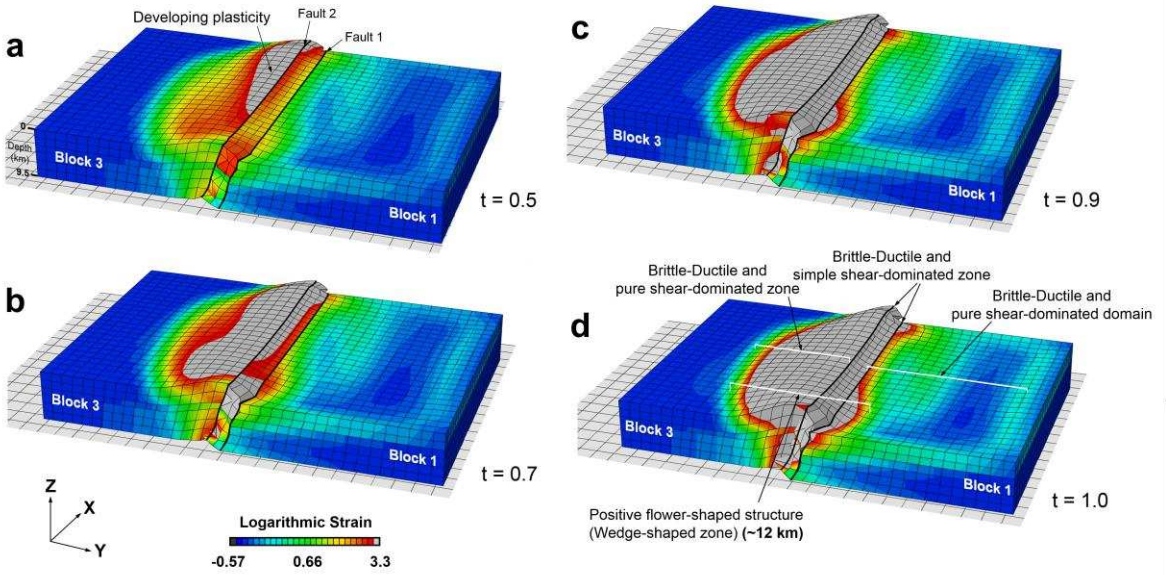

1052

1053 **Fig. 6.** Surface topography and interpretation of the magnitude and distribution of progressive
1054 deformation in the FE-model at different time steps a) 0.5, b) 0.7, c) 0.9, and d) 1.0 intervals
1055 of ca. 8%, 11%, 12%, and 16%, respectively (same strain bar scale for all models). Since
1056 nonlinear geometric effects are active, an efficient measure of strain is the logarithmic strain.
1057 The imposed plastic behaviour implies that in order to suffer permanent deformation the
1058 material must attain its passed yielding point (which is evaluated by comparing maximum Von
1059 Mises stress and yield stress at each element).

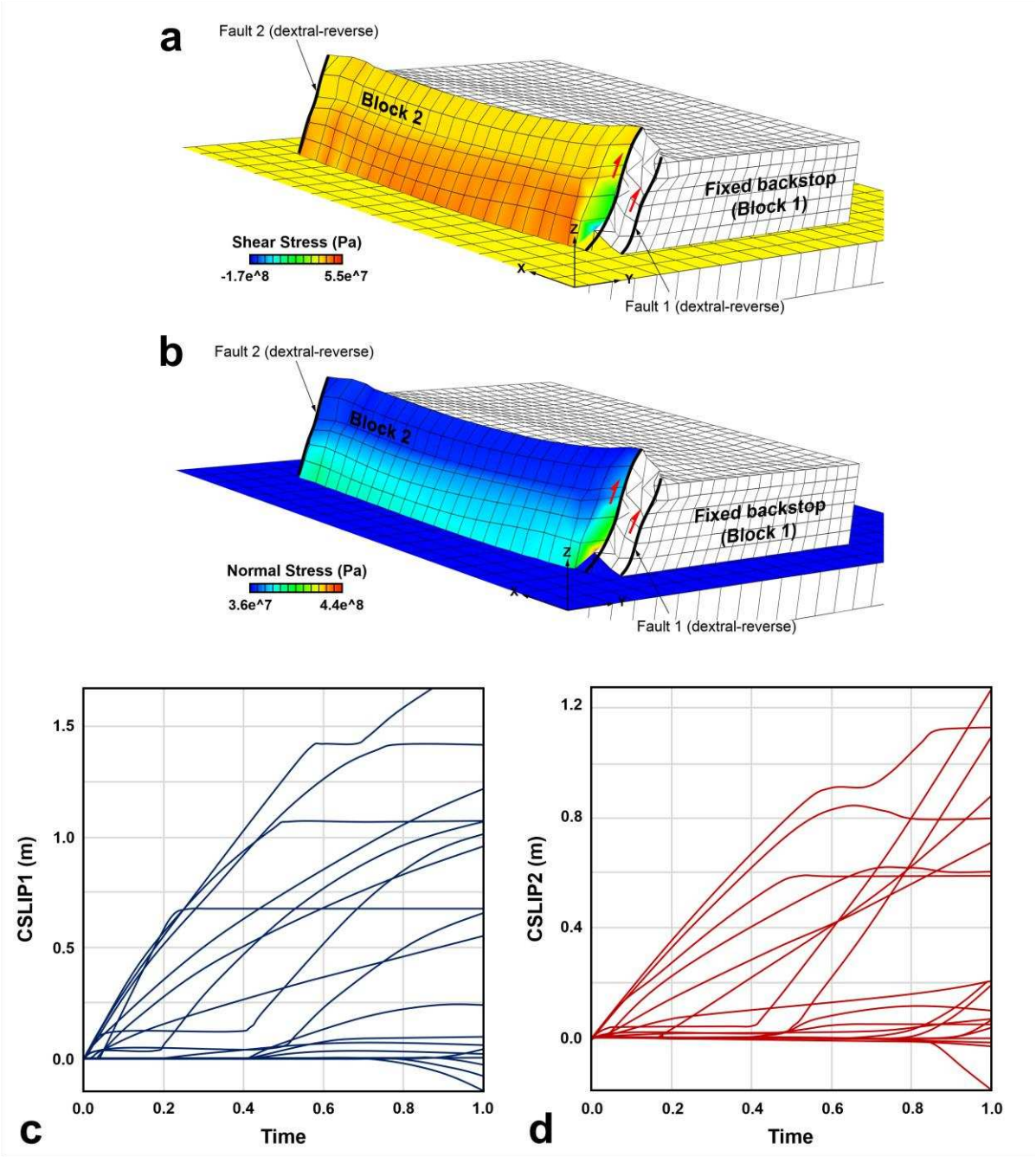

Fig. 7. Modelling results of distribution of a) shear stress; and b) normal stress along fault 2. c) Variations in shear strain along the versus time (with increasing oblique convergence). d, e) Variations in slip magnitude versus time (increasing oblique convergence). In 3D FE-models, there are two orthogonal slip directions along- and across-strike of fault 2 (CSLIP1 and CSLIP2 in ABAQUS^{TM}) for each point at a given contact surface, which together with the surface normal form an orthogonal coordinate system at every point on the surface, and therefore higher slip values resulted in higher nodal displacement. Negative magnitudes of CSLIP indicate that the node has moved in the negative slip direction.

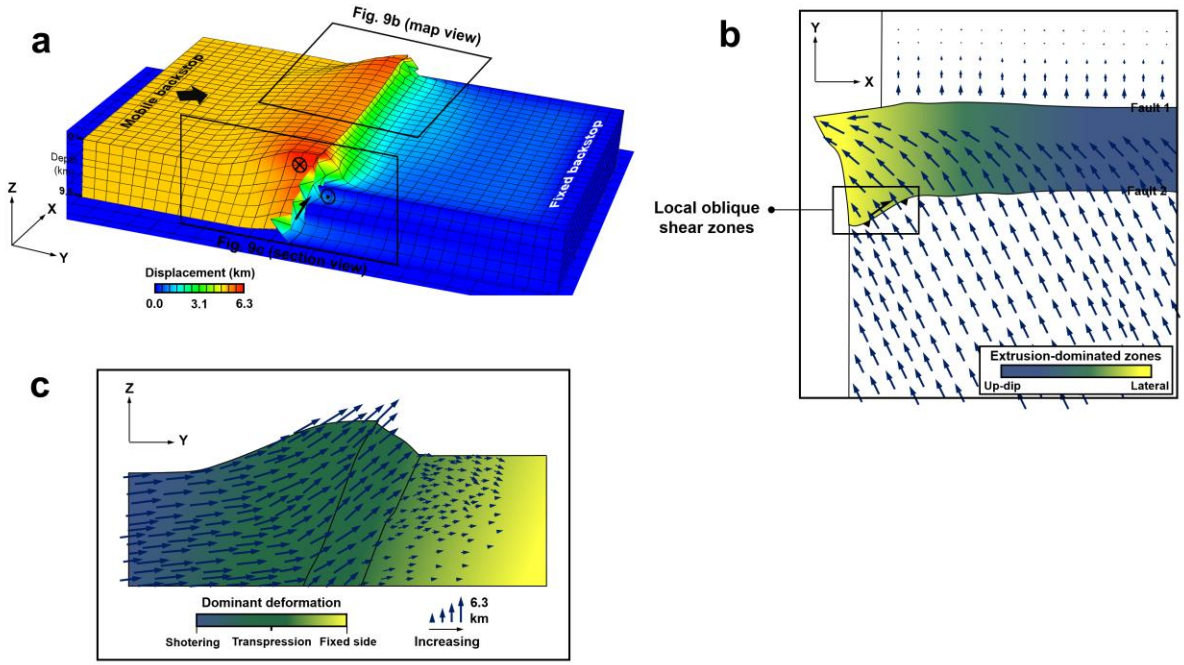

1069

1070 **Fig. 8.** a) Modelling result for displacement distribution. b) Top-view interpretation of
1071 displacement vectors within selected part of Fig. 7a, according to the colour spectrum, the
1072 transition from the central part of the transpression zone to its lateral part is characterized by a
1073 gradual transition of strain regime giving place to lateral extrusion. c) Section view
1074 interpretation of displacement vectors within selected part in Fig. 7a. According to the colour
1075 spectrum, the displacement vectors gradually deviate from the outer parts of the mobile block
1076 (block 3, left part of the section) to the transpression zone, so that angle between the
1077 displacement vectors gradually increases with respect to the Y-axis.

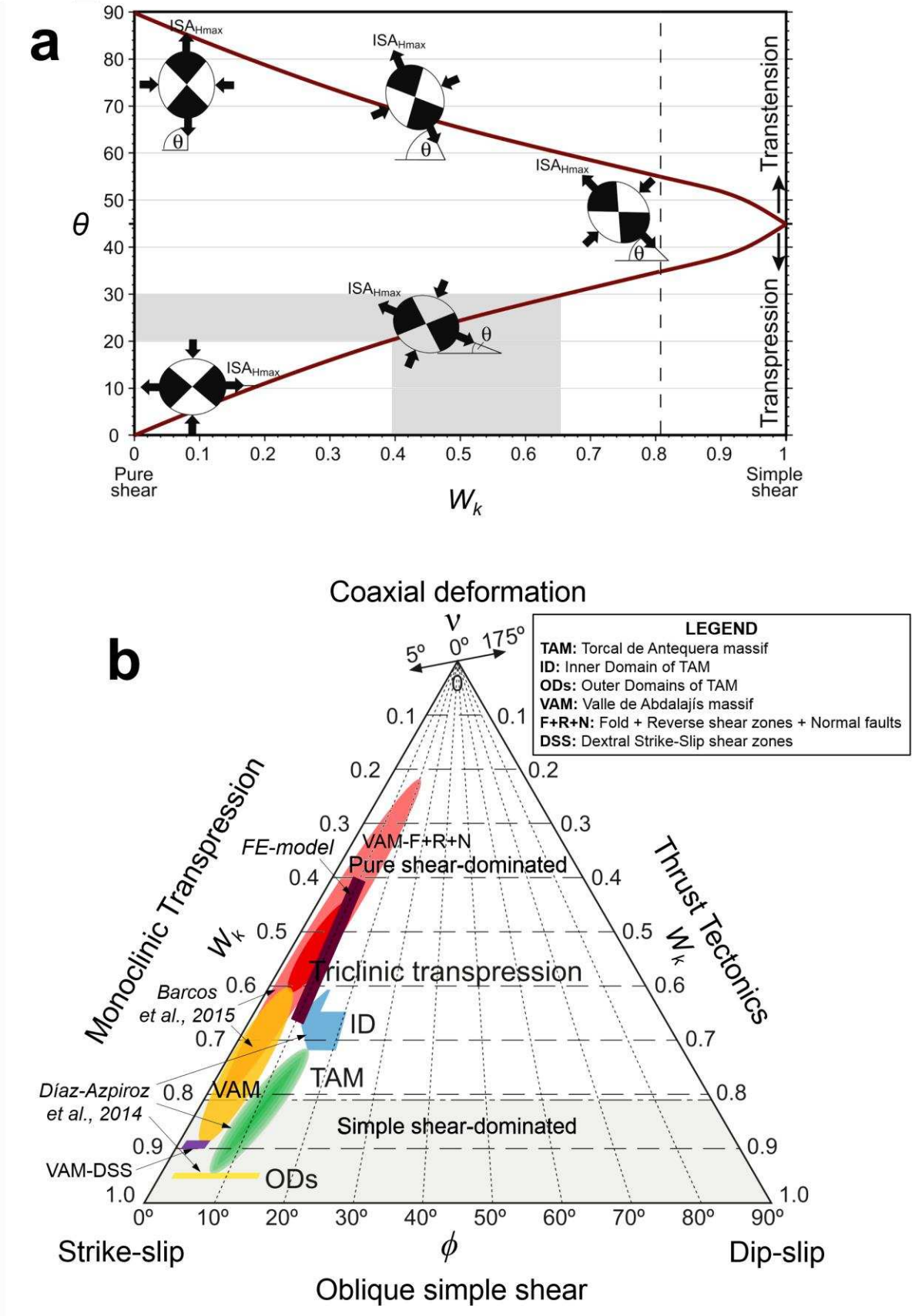
a
θ
W_k
Pure shear
Simple shear
Transtension
Transpression
ISA$_{Hmax}$
b
Coaxial deformation
Oblique simple shear
Strike-slip
Dip-slip
Monoclinic Transpression
Thrust Tectonics
W_k
ϕ
ν
5°
0°
175°
LEGEND
TAM: Torcal de Antequera massif
ID: Inner Domain of TAM
ODs: Outer Domains of TAM
VAM: Valle de Abdalajís massif
F+R+N: Fold + Reverse shear zones + Normal faults
DSS: Dextral Strike-Slip shear zones
FE-model
VAM-F+R+N
Pure shear-dominated
Triclinic transpression
Barcos et al., 2015
ID
TAM
Díaz-Azpiroz et al., 2014
VAM
Simple shear-dominated
VAM-DSS
ODs

1078

Fig. 9. a) Relationship between θ (angle of convergence of Fossen et al., 2013; which equal the value of angle α considered in this work) and W_k (kinematic vorticity number) (after Fossen et al., 2013). b) Strain partitioning within the study finite element model as viewed in a strain triangle proposed by Díaz-Azpiroz et al. (2014) inspired in that Jones et al. (2004), where FE-modelling results (dark purple line) compared with the kinematic transpression parameters for bulk strain within the Torcal de Antequera massif (Díaz-Azpiroz et al., 2014), and the Valle de Abdalajís massif (Barcos et al., 2015).

Table caption

Table 1. Summary of material properties and parameters used in the inclined transpression zone model.